Electron spin, kinetic energy, and stereodynamics control of the reaction between 9-methyl-8-oxoguanine radical cation and nitric oxide

Jonathan Benny[a,b] and Jianbo Liu*[a,b]
[a] Department of Chemistry and Biochemistry, Queens College of the City University of New York,
65-30 Kissena Blvd., Queens, NY 11367, USA
[b] The Ph.D. Program in Chemistry, the Graduate Center of the City University of New York,
365 5th Ave., New York, NY 10016, USA

Abstract 8-oxoguanine (OG) is a prevalent DNA lesion and exhibits a significantly lower oxidation potential than natural nucleic acid components, making the formation of $OG^{\bullet+}$ radical cation the most efficient hole trap in the one-electron oxidation of DNA. Nitric oxide ($^{\bullet}NO$) is a precursor to reactive nitrogen species and plays multiple roles in biological activities, including DNA base nitrosation and enhancement of DNA radiosensitivity in radiotherapy. Herein we report the reaction of $^{\bullet}NO$ with 9-methyl-8-oxoguanine radical cation ($9MOG^{\bullet+}$), a model compound for $OG^{\bullet+}$ nucleoside. $9MOG^{\bullet+}$ was generated via redox dissociation of $[Cu^{II}(9MOG)_3]^{\bullet 2+}$, and its reaction with $^{\bullet}NO$ was investigated using electrospray ionization guided-ion beam mass spectrometry as a function of kinetic energy. Multiple coupled reaction potential energy surfaces were computed using spin-projected ωB97XD, DLPNO-CCSD(T), and CASPT2 methods, with theoretical results benchmarked against experimentally determined reaction thermodynamics. The synergistic experiment and computation revealed distinct reaction mechanisms and dynamics across the open-shell singlet, close-shell singlet, and triplet states formed in radical-radical collisions. Comparison with the reaction of $^{\bullet}NO$ with guanine radical cation ($G^{\bullet+}$) (*J. Chem. Phys.*, 2023, **159**, 085102; 2024, **161**, 125101) addressed the resemblances and distinctions between $^{\bullet}NO$ reaction dynamics with $OG^{\bullet+}$ vs. $G^{\bullet+}$. On one hand, both systems present spin-orbit charge transfer, forming vibrationally excited $NO^+(v^+ = 1)$ product ions. On the other hand, $OG^{\bullet+}$ demonstrates lower nitrosation efficiency than $G^{\bullet+}$ due to few pathways, less favorable thermodynamics, and constrained stereodynamics. Only the closed-shell singlet $[5\text{-}NO\text{-}9MOG]^+$ product was detected. This study provides new insights into $^{\bullet}NO$-mediated DNA damage.

---

* Corresponding author email: jianbo.liu@qc.cuny.edu. Tel: 1-718-997-3271.

I. Introduction

Nitric oxide ($^{\bullet}$NO), produced from L-arginine by nitric oxide synthases in humans, plays diverse roles in physiological processes, including neurotransmitter, vasorelaxation, platelet aggregation inhibition, and host defense mechanisms.[1] In the human body, $^{\bullet}$NO is constitutively generated at a rate of 1×10^{-3} mol/day, but its level increases by 1–2 orders of magnitude during bacterial infections or inflammation.[2] Excessive $^{\bullet}$NO promotes the nitrosation[2] and deamination[3] of DNA bases, contributing to DNA strand breaks and cross-links[4] and ultimately culminating in mutation[4, 5] and carcinogenesis.[6] On the other hand, the DNA damage induced by $^{\bullet}$NO has long been harnessed to enhance radiogenic killing of anoxic bacteria[7] and improve radiotherapy of hypoxic tumor cells.[8, 9] The mechanism of $^{\bullet}$NO radiosensitization is not clearly understood. Radiation can produce radicals in cellular DNA — the presumed target for radiation-induced cell killing. It was proposed that the unpaired electron of $^{\bullet}$NO is able to pair up with DNA radical species generated by ionizing radiation, forming adducts that are toxic and, if not repaired, will result in the death of the cell.[7, 10-13] However, few experiments had identified distinct reaction pathways and products.

Among the four natural DNA nucleobases, guanine is the most readily oxidized due to its lowest ionization energy (IE = 7.75 eV in the gas phase[14] and 4.42 eV in solution[15]) and oxidation potential ($E°$ *vs*. standard hydrogen electrode = 1.29 V[16]). We recently investigated the reactions of $^{\bullet}$NO with the radical cations of guanine ($G^{\bullet+}$) and 9-methylguanine ($9MG^{\bullet+}$).[17, 18] These reactions encompass electronic configurations of open-shell singlet, closed-shell singlet, and triplet, along with internal conversions (IC) and inter-system crossing (ISC). Consequently, the reactions depend on electronic and vibrational states and spin-orbit coupling, which collectively govern reaction pathways, kinetics, and products.

This work expands our investigation of $^{\bullet}$NO-DNA chemistry toward the 8-oxoguanine radical cation ($OG^{\bullet+}$). The motivation for choosing $OG^{\bullet+}$ is multifaceted. First, the formation of $G^{\bullet+}$ is the initial step in a cascade of biological sequelae in oxidative DNA damage, with a key transformation being its conversion to OG.[19] As a result, OG represents the most common DNA lesion.[20, 21] Second, OG holds significant biological relevance. OG is involved in G·C → T·A transversion mutations[22] and DNA-protein cross-links,[23] which compromise transcription and replication integrity.[24] OG has been implicated in neurological disorders such as Parkinson′s[25] and Alzheimer′s[26] diseases, and is viewed as a biomarker for oxidative genotoxicity in cells and tissues.[27] Third, compared to G, OG has an $E°$ lower by 0.55 eV[28] and IE lower by 0.59[29] eV in the gas phase and 0.4 eV[29] in an aqueous environment, and is thus even more easily oxidized. Consequently, $OG^{•+}$ is the most effective hole trap, or oxidative damage sink, in the one-electron oxidation of DNA,[30] making it more susceptible to $^{•}NO$ under oxidative environments.

In this work, we used 9-methyl-8-oxoguanine (9MOG) as a model compound, with the methyl group serving as a structural proxy for the ribose sugar in 8-oxo-2′-deoxyguanosine. The charge transfer (CT) and nitrosation of $9MOG^{•+}$ and its monohydrate $9MOG^{•+}\cdot H_2O$ with $^{•}NO$ were examined as a function of reaction kinetic energy. Reaction potential energy surfaces (PESs) were computed across a wide interaction distance, dissecting the roles of open-shell singlet, closed-shell singlet, and triplet states throughout the reaction. The combined experimental and theoretical results unveiled distinct reaction pathways, key intermediates and products, and their dependence on charge, spin, and stereodynamics.

II. Experimental Details

A. Chemicals and instrumentation

9MOG was kindly provided by Dr. Lippert (University of Dortmund, Germany), and its synthesis was reported.[31] 2′-deoxyguanosine (dGuo, Sigma-Aldrich, > 99%), $Cu(NO_3)_2$ (Alfa Aesar, 99.999%), methanol (Fisher, HPLC grade), water (J. T. Baker, HPLC grade), and $^{•}NO$ gas (Linde, > 99.5%) were utilized without further purification. Reactions were carried out on a home-built guided-ion beam mass spectrometer.[32] The apparatus comprises of an electrospray ionization (ESI) source, a radiofrequency (rf) hexapole ion guide, a reactant-selection quadrupole mass filter, a rf octopole ion guide surrounded in the central section by a scattering cell, a product quadrupole mass filter, and an electron multiplier detector.

A redox separation reaction of $[Cu^{II}(nucleobase)_3]^{•2+} \rightarrow [Cu^{I}(nucleobase)_2]^{+} + nucleobase^{•+}$ was utilized as a source for generating nucleobase radical cations.[33-37] A fresh solution was prepared by mixing equimolar (0.25 mM) $Cu(NO_3)_2$, 9MOG, and dGuo in 3:1 (v:v) methanol/water, of which dGuo was intended to enhance the formation of $9MOG^{\bullet+}$ during complex dissociation.[37] The solution was electrosprayed at a flow rate of 0.06 mL/hr. The Cu^{II}-nucleobase complexes were directed into the source chamber of the mass spectrometer via a heated (190 °C) desolvation capillary. A 1.0-mm-orifice skimmer, positioned at 3 mm from the end of the capillary, separates the source chamber and the hexapole ion guide. The skimmer and capillary were biased at +19 V and +155 V, respectively. The electric field between them prompted collision-induced dissociation of Cu^{II}-nucleobase complexes with the background gas in the source chamber (1.6 Torr pressure), resulting in $9MOG^{\bullet+}$ at an intensity of 1.2×10^5 counts per sec (cps). Upon mild heating of the desolvation capillary (160 °C), monohydrated $9MOG^{\bullet+}\cdot H_2O$ formed at an intensity of 8×10^3 cps.

Radical cations were directed through the hexapole ion guide by a combination of rf and DC potentials, and meanwhile, experienced collisional focusing and energy dumping[38] (with background gas at a pressure of ~20 mTorr), resulting in ion beam collimation and thermalization to 310 K.[32] Radical ions of interest were mass selected by the first quadrupole mass filter and introduced into an octopole ion guide, which guided ions through an 11-cm-long scattering cell filled with the $^{\bullet}NO$ gas. The octopole was also operated using rf and DC potentials. The rf potential confined ions in the radial direction, while the DC potential accelerated/decelerated ions at the octopole entrance, controlling ion kinetic energy in the laboratory frame (E_{lab}). The center-of-mass collision energy (E_{CM}) was calculated using $E_{CM} = E_{lab} \times m_{neutral}/(m_{neutral} + m_{ion})$, where m_{ion} and $m_{neutral}$ represent the masses of ionic and neutral reactants, respectively. The full width at half-maximum (FWHM) and absolute zero of E_{lab} were calibrated using a retarding potential measurement.[32] The FWHM of E_{lab} was 0.55 eV, which corresponded to a spread of 0.09 eV for E_{CM}. Reactions were examined across an E_{CM} range of 0.02 to 6.0 eV. Product ions, along with remaining reactant ions, were collected by the octopole and focused into the second quadrupole mass filter for analysis and registered using the pulse-counting detector.

The $^{\bullet}NO$ pressure in the scattering cell was maintained at ≤ 0.036 mTorr. Under these conditions, the probability of single ion-molecule collisions was 4%, while the likelihood of multiple collisions remained below 0.2%. Consequently, reaction cross sections were determined based on the ratio of product to reactant ion intensities, the target gas pressure, and the effective cell length for collisions, following the Beer-Lambert law.[39] Each measurement was repeated six times to evaluate relative uncertainties.

B. Analysis of 0 K reaction threshold

The E_{CM} dependence of the CT cross section was modeled by a modified line-of-centers (LOC) theory:[39-43] $\sigma(E_{\mathrm{CM}}) = \sigma_0(E_{\mathrm{CM}} + E_{\mathrm{vib}} + E_{\mathrm{rot}} - E_0)^n/E_{\mathrm{CM}}$, where σ_0 is a normalization factor, E_{vib} and E_{rot} are reactants′ vibrational and rotational energies, and n is an adjustable parameter that controls the curvature of $\sigma(E_{\mathrm{CM}})$. A leveling-off function was applied to ensure that the cross section eventually reaches a plateau. To account for the energy spread in E_{CM}, the Boltzmann distributions of E_{vib} and E_{rot}, the Doppler broadening of the neutral target,[44] and reaction kinetic shift,[45] the LOC model was integrated into a Monte Carlo ion-molecule collision simulation program designed to replicate experimental conditions.[46, 47] E_0 was determined from simulations that best matched the experimental cross section.

III. Computational Methods

A. Structure optimization using density functional theory (DFT)

Geometries of reactants, intermediate complexes, transition states (TSs), and products were optimized at the ωB97XD/6-31+G(d,p) level using Gaussian 16.[48] The ωB97XD functional mitigates self-interaction errors and improves the description of radicals.[49] All TS structures are featured by a single imaginary frequency, and intrinsic reaction coordinate was calculated to verify that each TS connects to the correct reactant and product pair. To distinguish between open- and closed-shell singlet structures, open-shell singlet was calculated utilizing the broken symmetry (BS) unrestricted SCF approach, with ″guess = mix″ to mix HOMO and LUMO and break α-β and spatial symmetries;[50] whereas closed-shell singlet was calculated using restricted SCF. Energies of singlet diradicals were spin-purified using Yamaguchi′s approximate spin-projection method:[17, 51-53] $E^{\mathrm{AP}} = \frac{\langle \hat{S}^2\rangle^{\mathrm{HS}}}{\langle \hat{S}^2\rangle^{\mathrm{HS}} - \langle \hat{S}^2\rangle^{BS}} E^{BS} - \frac{\langle \hat{S}^2\rangle^{\mathrm{BS}}}{\langle \hat{S}^2\rangle^{\mathrm{HS}} - \langle \hat{S}^2\rangle^{\mathrm{BS}}} E^{\mathrm{HS}}$, where E^{BS} and $\langle \hat{S}^2\rangle^{\mathrm{BS}}$ denote the energy and the expectation value of the total spin angular momentum operator for the BS singlet, while E^{HS} and $\langle \hat{S}^2 \rangle^{\mathrm{HS}}$ correspond to the triplet values. Calculated reaction enthalpy at 0 K, ΔH (0 K), includes zero-point energy (ZPE, scaled by 0.975[54]), and ΔH (298 K) includes thermal correction. Atomic charge and *α*- and *β*-spin distributions were analyzed using NBO 6.0.[55]

To identify the low-energy isomers and global minimum structure of the $9\mathrm{MOG}^{\bullet+}\cdot\mathrm{H_2O}$ cluster, a random search procedure ("RAND")[56] in Q-CHEM 5.0[57] was used in conjunction with the ωB97XD/6-31+G(d) theory. In each search, the $9\mathrm{MOG}^{\bullet+}$ moiety was fixed in position while the H_2O molecule underwent 20 random rotations and translations.[58] A total of 200 structures were generated. Their energies were refined at the ωB97XD/6-31+G(d,p) level, and frequency calculations confirmed the structures corresponded to true minima on the potential energy surface.

The unrestricted and restricted open-shell ωB97XD/6-31+G(d,p) overestimated the adiabatic ionization energy (AIE) of $^{\bullet}$NO by 0.48 and 0.44 eV, respectively, compared to the experimental AIE($^{\bullet}$NO) of 9.2643 ± 0.0005 eV.[59] The discrepancy arises from the triplet instability associated with the unrestricted wave function of doublet $^{\bullet}$NO,[60, 61] in which spin pairing in the Hartree-Fock wave function breaks down, leading to significant spin polarization and strong spin contamination. The Linnett double-quartet theory[62, 63] provided an alternative view of electronic configuration for $^{\bullet}$NO, *i.e.*, $[\bullet\,{}^{\times}_{\times}N^{\times}_{x}\overset{\bullet}{\underset{\bullet}{\bullet}}O^{\times}_{\times}\,\bullet]$ with 5 electrons of one spin and 6 electrons of the other. In this work, the DFT energy of $^{\bullet}$NO was obtained by subtracting the experimental AIE($^{\bullet}$NO) from the DFT energy of NO^+.[17, 18]

B. Spin contamination evaluated by coupled-cluster theory

In addition to evaluating $\langle \hat{S}^2 \rangle$ values, spin contamination was assessed using T1 diagnostics.[64, 65] The $T1$ value is defined as $\|t_1\|/\sqrt{N}$, *i.e.*, the Frobenius norm (or the Euclidean norm of the matrix) of the single-excitation amplitude vector (t_1) of the coupled-cluster wave function, normalized by the square root of the number of correlated electrons (N).[64] Typically, single-configuration closed-shell and open-shell systems exhibit $T1$ values below 0.02 and 0.03, respectively, whereas values above 0.06 indicate moderate multireference character, and those exceeding 0.16 suggest severe multireference effects.[66]

T1 diagnostics for DFT-optimized structures were performed at the domain-based local pair-natural orbital coupled-cluster single-, double-, and perturbative triple-excitations, DLPNO-CCSD(T),[67] paired with the aug-cc-pVTZ basis set using ORCA 4.2.[68] The inclusion of a perturbative correction for triple excitation mitigates deficiencies of a single-determinant reference, allowing DLPNO-CCSD(T) to effectively manage moderate spin contamination. Consequently, the DLPNO-CCSD(T)-calculated AIE($^{\bullet}$NO) (9.20 eV) is only 0.06 eV less than the experimental value.

C. Energy refinement using multireference approaches

To assess the reliability of spin-projected DFT and DLPNO-CCSD(T), the system was analyzed using complete active space self-consistent field (CASSCF)[69] paired with ANO-RCC-VTZP orbitals acquired from the Basis Set Exchange.[70] Active spaces were (9,7) for 9MOG$^{\bullet+}$, (11,8) for $^{\bullet}$NO, and (20,15) for adducts, incorporating $\sigma_{O(2s)\text{-}N(2s)}$, $\sigma^*_{O(2s)\text{-}N(2s)}$, $2 \times \pi_{O(2p)\text{-}N(2p)}$, $\sigma_{O(2p)\text{-}N(2p)}$, $2 \times \pi^*_{O(2p)\text{-}N(2p)}$, and $\sigma^*_{O(2p)\text{-}N(2p)}$ in $^{\bullet}$NO, and π and $\sigma_{N\text{–}H}$ in 9MOG$^{\bullet+}$. However, CASSCF significantly underestimated AIE($^{\bullet}$NO) by 1.7 eV,[18] likely due to its limited treatment of dynamic electron correlation. To address dynamic correlation, we used complete active space second-order perturbation theory (CASPT2)[71, 72] paired with ANO-L-VTZP. The CASPT2-calculated AIE($^{\bullet}$NO) of 9.06 eV is 0.2 eV lower than the experimental value.

CASSCF calculations were conducted using Gaussian 16. CASPT2 calculations were executed utilizing OpenMolcas 23.10.[73] A shift parameter for ionization potential-electron affinity (0.25 a.u.)[74] was applied to balance descriptions of open- and closed-shell configurations in the zeroth-order Hamiltonian.[75] Reaction enthalpies reported at DLPNO-CCSD(T) and CASPT2 include the electronic energy calculated at the respective level of theory and thermal correction derived from ωB97XD/6-31+G(d,p) calculations.

D. Spin-orbit coupling between time-dependent DFT states

Spin-orbit coupling constants (SOCCs) were calculated using time-dependent ωB97XD/6-31+G(d) within the Tamm-Dancoff approximation (TDA)[76] and standard spin-conserving formulation, implemented in Q-CHEM. Both one-electron (considering orbital angular momentum and spin of a single electron only)[77] and mean-field (an averaged spin-orbit coupling across all electrons, incorporating the electronic environment via a mean-field approximation)[77] SOCCs were evaluated. The Breit-Pauli Hamiltonian and Wigner-Eckart theorem were applied to the reduced one-electron transition density matrices, with a mean-field treatment of the two-electron contribution to the Breit-Pauli Hamiltonian.[78]

IV. Experimental Results

A. Structures of $9MOG^{\bullet+}$, $9MOG^{\bullet+}\cdot H_2O$, and $^{\bullet}NO$

Neutral 9MOG exhibits multiple tautomers and rotamers resulting from keto-enol and amino-imino isomerizations, with the 6,8-diketone structure being the most prevalent, followed by the 6-enol-8-ketone structure.[79] Similar to its neutral counterpart, $9MOG^{\bullet+}$ adopts the 6,8-diketone structure as its global minimum;[37] and the *anti*- and *syn*-6-enol-8-keto tautomers are 0.17 and 0.81 eV higher in energy, making them insignificant in the reaction. Scheme 1 presents the NBO charge and spin density distributions for $9MOG^{\bullet+}$ and $^{\bullet}NO$. In $9MOG^{\bullet+}$, spin is primarily delocalized across the N3, C4, C5, and N7 sites, with minor spreading around N2, O6, and O8; and positive charge is mostly centered at C4–C5 (total $\delta^+ = 0.59$) and C8 ($\delta^+ = 0.83$). $9MOG^{\bullet+}$ presents nearly identical spin and charge distributions as those of 8-oxo-2′-deoxyguanosine radical cation,[37] suggesting that N9-methyl substitution is unlikely to alter the nucleoside nitrosation mechanism. But $9MOG^{\bullet+}$ greatly simplified product analysis and computational modeling. $^{\bullet}NO$ exhibits charge separation, with $\delta^- = -0.21$ on the N atom and $\delta^+ = 0.21$ on the O atom.

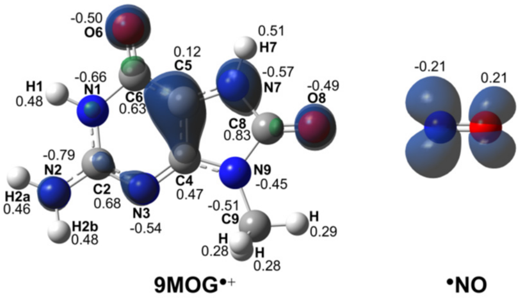

Scheme 1. Structures of $9MOG^{\bullet+}$ and $^{\bullet}NO$, with atomic numbering. Spin (represented by contour plots) and atomic charge (values) were calculated using NBO 6.0 at the ωB97XD/6-31+G(d,p) level.

Low-energy structures of the $9MOG^{\bullet+}\cdot H_2O$ reactant were identified using random search[56, 58] followed by ωB97XD/6-31+G(d,p) optimization, and are illustrated in Scheme 2. Hydration enthalpy ($\Delta H_{hydration}$) is -0.68 eV for $9MOG^{\bullet+}\cdot W12$ (water doubly H-bonded to N1-H and N2-H), decreasing to -0.61 eV for

$9MOG^{\bullet+}\cdot W67$, -0.58 eV for $9MOG^{\bullet+}\cdot W16$, and -0.47 eV for $9MOG^{\bullet+}\cdot W2$. Ion-dipole complexes, such as $9MOG^{\bullet+}\cdot W9$, also exist. Thermal populations are 0.92 for $9MOG^{\bullet+}\cdot W12$, 0.06 for $9MOG^{\bullet+}\cdot W67$, and 0.02 for $9MOG^{\bullet+}\cdot W16$, with all others being negligible.

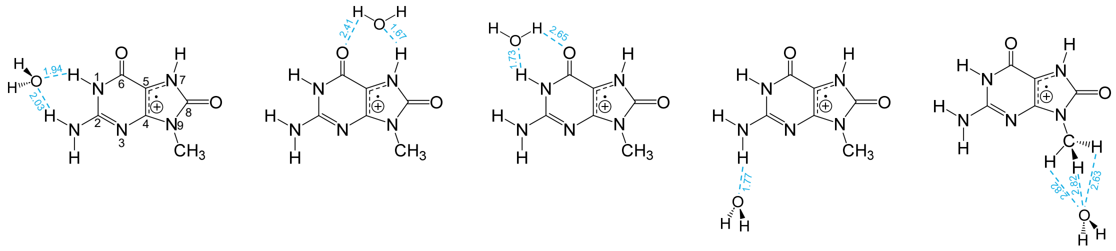

$9MOG^{\bullet+}\cdot W12$ 0.00 ($\Delta H_{hydration}$ = -0.68)
$9MOG^{\bullet+}\cdot W67$ 0.07 (-0.61)
$9MOG^{\bullet+}\cdot W16$ 0.10 (-0.58)
$9MOG^{\bullet+}\cdot W2$ 0.21 (-0.47)
$9MOG^{\bullet+}\cdot W9$ 0.48 (-0.20)

Scheme 2. Conformers of $9MOG^{\bullet+}\cdot H_2O$, along with atom numbering and nomenclature. Hydration sites are indicated by the last two numbers in the nomenclature. H-bonds are depicted as blue dashed lines with length given in Å. Energies (eV, relative to the global minimum) and hydration enthalpies (in parentheses) were calculated at the DLPNO-CCSD(T)/aug-cc-pVTZ//ωB97XD/6-31+G(d,p) levels.

B. Charge transfer between $9MOG^{\bullet+}$ and $^{\bullet}NO$

We first investigated CT between $9MOG^{\bullet+}$ and $^{\bullet}NO$ by measuring its product ions over an energy range of 0.5 to 6.0 eV in the center-of-mass frame. The cross section for the NO^+ product ion is shown in Figure 1a, with error bars representing standard deviations from six independent measurements. The cross section rises from zero at an E_{CM} between 2 and 3 eV, increases with energy, and levels off around 6 eV, consistent with an endothermic process.

Since the calculated threshold for forming triplet 9MOG in the CT reaction is 4.88 eV but no additional product channel was observed around that region, we can rule out this possibility and conclude that the CT reaction produced 9MOG (singlet) + NO^+ exclusively. Theoretically, the CT threshold energy is determined by the difference between the AIE values of the reactants. Currently, no photoionization data is available for 9MOG. Computation at the composite DLPNO-CCSD(T)/aug-cc-pVTZ//ωB97XD/6-31+G(d,p) levels of theory predicts AIE(9MOG) to be 7.37 eV. Note that the same method yields AIE(G) of 7.78 eV, which is within 0.03 eV of the experimentally measured AIE(G) of 7.75 eV via VUV photoionization efficiency spectroscopy.[14] This close agreement suggests that the calculated AIE(9MOG) has a similar level of accuracy. AIE ($^{\bullet}NO$) was determined to be 9.2643 ± 0.0005 eV using pulsed-field ionization photoelectron spectroscopy.[59] Using these AIE values, the 0 K adiabatic CT threshold for reaction (1) is calculated as:

$$9MOG^{\bullet+} + {}^{\bullet}NO \rightarrow 9MOG\ (singlet) + NO^{+}(\nu^{+} = 0) \qquad \Delta H\ (0\ K) = 1.89\ eV \qquad (1)$$

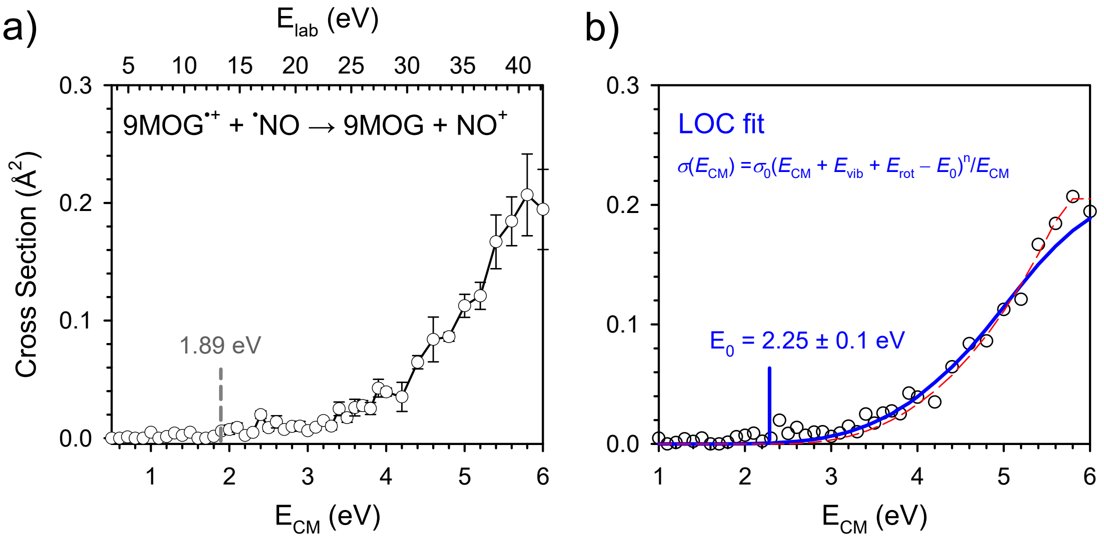

Figure 1. a) Product ion (NO^+) cross section for the charge transfer reaction of $9MOG^{\bullet+}$ + $^{\bullet}NO$, plotted as a function of center-of-mass collision energy (E_{CM}, bottom axis) and laboratory-frame kinetic energy (E_{lab}, top axis). The gray vertical line marks 0 K adiabatic threshold energy; and b) LOC fitting of the product ion cross section, where the blue solid line represents the convoluted LOC cross section incorporating reactant internal and kinetic energy distributions, while the red dashed line shows the LOC cross section without energy broadening. The best-fitted threshold energy is indicated by the blue vertical line.

The 0 K adiabatic threshold is indicated by the gray dashed line in Figure 1a. Surprisingly, the adiabatic threshold lies below the apparent onset of the cross section. To quantify the energy shift between the 0 K adiabatic CT threshold and the actual threshold, we must consider the kinetic energy spread of the primary ion beam, the thermal motion of $^{\bullet}NO$, and the kinetic shift in the reaction. To address these effects, the LOC model was used to account for all reaction energy sources and convoluted over energy broadening factors. To reproduce the experimental cross section, multiple sets of LOC fits were performed with the E_0 and n values adjusted independently for each set. The best-fit LOC curve is shown as the blue solid curve in Figure 1b, from which an E_0 value of 2.25 eV was extracted. An uncertainty of 0.1 eV was determined through multiple fits across an acceptable range of n (= 2.5 – 3.5), and by accounting for the absolute uncertainty in E_{CM}. In a canonical LOC model, n (which controls the curvature of the cross-section rise near threshold) is 1.0; however, values of ≥ 2 are required to reproduce the concave-up (quadratic) increase in cross section. The physical significance of the n value greater than unity depends on the reaction mechanisms and the nature of TS for a translationally driven reaction.[41] A high n value may indicate a long-lived intermediate complex[40] or an orientation-dependent activation barrier and significant steric factor,[42] as discussed below.

The comparison between the adiabatic and experimental CT thresholds reveals a difference of 0.36 eV, which exceeds the combined uncertainty of 0.1 eV in the experiment. This difference provides important insight into the CT dynamics. A similar phenomenon was observed in the CT reactions of $G^{\bullet+}$ + $^{\bullet}NO$ and $9MG^{\bullet+}$ + $^{\bullet}NO$,[17] where the experimental thresholds were 0.24 and 0.37 eV above the 0 K product asymptotes of G + NO^+ and 9MG + NO^+, respectively. The additional threshold energies can be rationalized through the Franck-Condon factor (FCF) in the ionization of $^{\bullet}NO$ ($X^2\Pi$) to NO^+ ($X^1\Sigma^+$). Due to the bond length contraction upon ionization (rNO = 1.151 Å *vs.* rNO^+ = 1.064 Å),[80] the FCF for forming $NO^+(v^+ = 0)$ is only 0.16, increasing to 0.30 – 0.33 for $v^+ = 1$ (E_{vib} = 0.29 eV) and 2 (0.577 eV) as rNO^+ expands, then decreasing to 0.15 for $v^+ = 3$ (0.859 eV) and 0.05 for $v^+ = 4$ (1.137 eV). Consequently, photoionization exhibits a long progression of vibrational excitation in $NO^+(X^1\Sigma^+)$.[59] In the CT reactions of $^{\bullet}NO$ with $9MOG^{\bullet+}$, $9MG^{\bullet+}$, and $G^{\bullet+}$, the ~0.3 eV shift above the 0 K adiabatic thresholds suggests that CT leads to the formation of vibrationally excited NO^+ with $v^+ = 1$. This implies that CT between $^{\bullet}NO$ and nucleobase radical cations facilitates resonant energy transfer. What remains unknown is which electronic state(s) are responsible for CT and how energy is partitioned into the NO^+ vibration (*i.e.*, the driving force).

We also calculated the hydrogen transfer and proton transfer reactions, considering all possible product pairs. All of these reactions are endothermic, and no products were detected in the experiment as a consequence of the very high reaction endothermicities and competition with charge transfer. This finding is similar to the case of $9MG^{\bullet+}$ + $^{\bullet}NO$.[17]

$9MOG^{\bullet+} + {}^{\bullet}NO$

$\rightarrow [9MOG - H_{N1}]^+ + {}^1HNO / {}^3HNO \qquad \Delta H\ (0\ K) = 2.04 / 2.79\ eV \qquad (2a)$

$\rightarrow [9MOG - H_{N1}]^+ + {}^1HON / {}^3HON \qquad \Delta H\ (0\ K) = 3.88 / 3.07\ eV \qquad (2b)$

$\rightarrow$ [9MOG – H_{N7}]$^+$ + ^{1}HNO / ^{3}HNO ΔH (0 K) = 1.30 / 2.04 eV (2c)

$\rightarrow$ [9MOG – H_{N7}]$^+$ + ^{1}HON / ^{3}HON ΔH (0 K) = 3.14 / 2.33 eV (2d)

$\rightarrow$ [9MOG – H_{N1}] + HNO^+ ΔH (0 K) = 4.42 eV (3a)

$\rightarrow$ [9MOG – H_{N1}] + HON^+ ΔH (0 K) = 5.12 eV (3b)

$\rightarrow$ [9MOG – H_{N7}] + HNO^+ ΔH (0 K) = 4.45 eV (3c)

$\rightarrow$ [9MOG – H_{N7}] + HON^+ ΔH (0 K) = 5.14 eV (3d)

C. Nitrosation of 9MOG$^{\bullet+}$

We then investigated the nitration reaction of 9MOG$^{\bullet+}$ with $^{\bullet}$NO. However, no nitrosation product was detected experimentally. One explanation for this absence is that nitrosation may be highly exothermic, leading to excess internal energy in the nascent product, which subsequently decays back into reactants. To mitigate this potentially unfavorable kinetics, we used monohydrated 9MOG$^{\bullet+}$·H_2O as the reactant ion in collisions with $^{\bullet}$NO. In this hydrated system, the nitrosation exothermicity, which might otherwise cause decomposition of the [9MOG·NO]$^+$ adduct, could instead facilitate water ligand elimination and kinetic energy release of the products.[36, 81]

Following this strategy, we measured the nitration of 9MOG$^{\bullet+}$·H_2O (*m/z* 199) at various energies. Product ions were detected at *m/z* 211 (see the inset mass spectrum in Figure 2), corresponding to the loss of water from the NO-adduct of 9MOG$^{\bullet+}$·H_2O. Figure 2 presents both product ion cross section and reaction efficiency as a function of E_{CM} from 0.05 to 1.0 eV. The reaction efficiency was calculated as $\sigma_{reaction}/\sigma_{collision}$, where $\sigma_{collision}$ is the larger of the ion-induced dipole capture cross section[82] and the hard-sphere collision cross section, the latter estimated using the orientation-averaged projected area method available in the IMoS program.[83] The cross section peaks at the lowest E_{CM} and declines as the energy increases, supporting our prediction that nitrosation is exothermic and barrierless. The maximum reaction efficiency is 0.16% at E_{CM} = 0.08 eV, quickly decreasing to 0.03% at E_{CM} = 0.5 eV. The apparent dip in the reaction efficiency at E_{CM} < 0.08 eV is an artifact caused by backscattering of some product ions at the lowest energy, leading to their escape from product ion detection. Based on the trend of reaction efficiency *vs.* E_{CM}, the actual efficiency is estimated to be 0.3 % at E_{CM} = 0.02 eV.

The low reaction efficiency of 9MOG$^{\bullet+}$·H_2O may partially stem from insufficient energy relaxation.

Even in a hydrated system, a significant portion of adducts may dissociate back into initial reactants before reaching the ion detector (within the ion time-of-flight window of 100 – 500 μs).[36, 84] Importantly, the exothermic pathway for $9MOG^{\bullet+}\cdot H_2O + {}^{\bullet}NO \rightarrow [NO\text{-}9MOG]^+ + H_2O$ establishes a lower limit for the accessible nitrosation pathways. That is, the reaction must be sufficiently exothermic — comparable to the $\Delta H_{hydration}$ of $9MOG^{\bullet+}\cdot H_2O$ — to be detected.

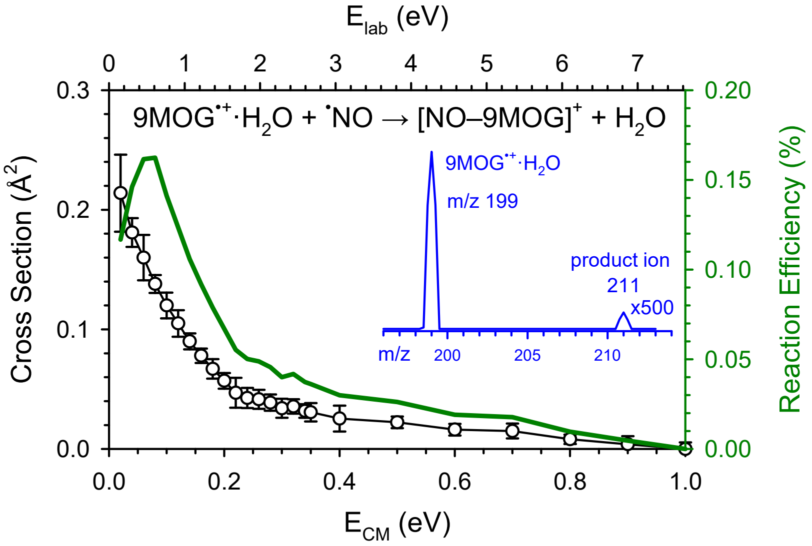

Figure 2. Product ion cross section with error bars (left axis) and reaction efficiency (right axis) for the nitrosation of $9MOG^{\bullet+}\cdot H_2O$ by $^{\bullet}NO$ as a function of kinetic energy, presented in the center-of-mass frame (E_{CM}, bottom axis) and laboratory frame (E_{lab}, top axis). Inset shows the product ion mass spectrum measured at E_{CM} = 0.02 eV, with the product ion intensity scaled by a factor of 500.

V. Discussion

A. Spin dependence

The profile of PES depends on the relative alignment of colliding partners, which dictates the access to reactive pathways. The most reactive orientation corresponds to the N-terminal of $^{\bullet}NO$ approaching the imidazole ring of $9MOG^{\bullet+}$, as the N-terminal carries the radical electron and exhibits higher reactivity than the O-terminal. Figure 3 presents a representative PES scanned along the distance between the center-of-mass of 9MOG and the N-terminal, r[9MOG−N], from 10 Å to 1.5 Å in increments of 0.02 Å. All bond lengths (except the scanning coordinate) and bond angles were optimized at each step using ωB97XD/6-31+G(d,p). The PES explores the open-shell singlet, closed-shell singlet, and triplet states, and the energy for the open-shell singlet was purified using approximate spin projection. To verify individual electronic state, $\langle\hat{S}^2\rangle$ was calculated along PES. The $\langle\hat{S}^2\rangle$ value remains 2.00 – 2.01 throughout the triplet surface, confirming a pure triplet state. For the open-shell singlet, the $\langle\hat{S}^2\rangle^{\mathrm{BS}}$ value is 1.00 within r[9MOG–N] of 3.8 – 10 Å, indicating a 100% diradical character based on the diradical index $n_{DC} = \left(1 - \sqrt{1 - \langle\hat{\boldsymbol{S}}^2\rangle^{\mathrm{BS}}}\right) \times 100\%$;[85] however, the value decreases as the reactants approach more closely, reaching 0.89 at r[9MG–N] = 3.0 Å, 0.80 at 2.7 Å, and 0.76 at 2.6 Å, before dropping to 0.0 at even shorter distances (see Supplementary Figure S1). This trend suggests that the open-shell singlet becomes unstable as reactants approach each other closely, ultimately converting into a closed-shell singlet.

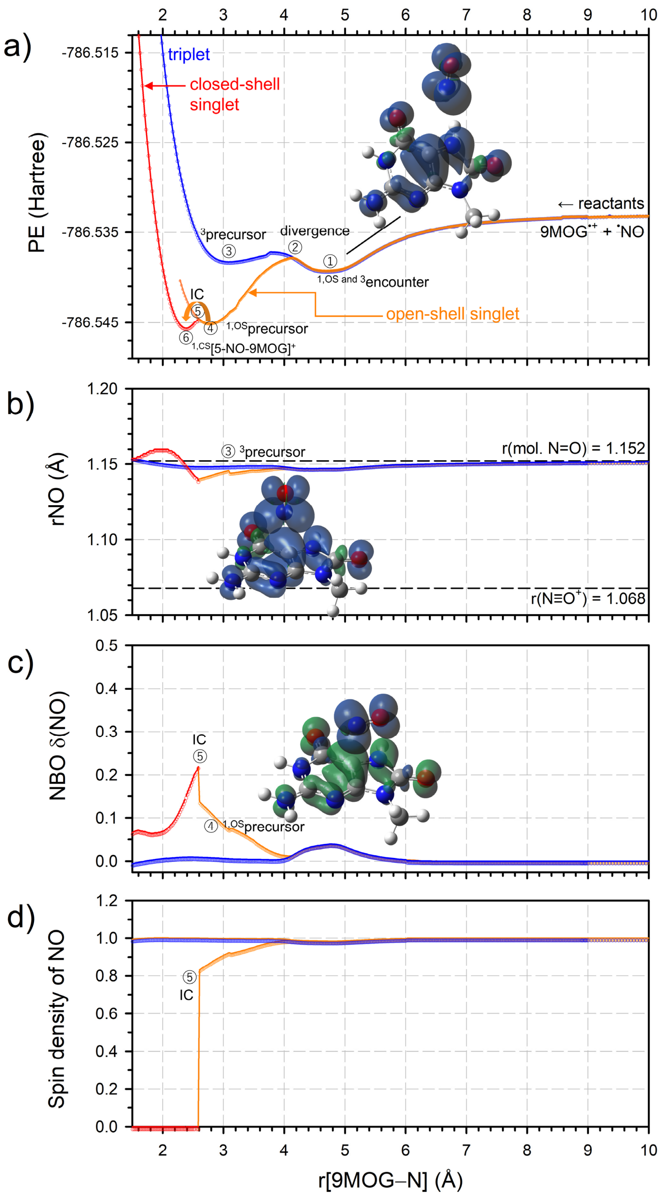

Figure 3. Relaxed PES for 9MOG$^{\bullet+}$ + $^{\bullet}$NO along r[9MOG−N], the distance between the center-of-mass of 9MOG$^{\bullet+}$ and the N-terminal of $^{\bullet}$NO, calculated at the ωB97XD/6-31+G(d,p) level. a) Changes in reaction potential energy; b) changes in the NO bond length, with horizontal dashed lines indicating equilibrium bond lengths of NO and NO^{+}; and c – d) changes in NBO charge and spin density of NO. Electronic states are distinguished by colors: red for closed-shell singlet, orange for open-shell singlet, and blue for triplet. Insets show representative structures (C: gray; H: white; N: blue; and O: red) along with density contour plots, where α and β spins are depicted in blue and green, respectively.

In the following, we analyze the PES based on the interaction range of the reactants.

1) Initial approach at long range. The radical pair forms either an open-shell singlet ^{1,OS}[9MOG$^{\bullet+}$(↑)⋯(↓)$^{\bullet}$NO] or a triplet ^{3}[9MOG$^{\bullet+}$(↑)⋯(↑)$^{\bullet}$NO]. Given that there is only one anti-symmetric singlet spin eigenfunction ($[\alpha(1)\beta(2) - \beta(1)\alpha(2)]/\sqrt{2}$) but three symmetric triplet spin eigenfunctions

($\alpha(1)\alpha(2)$, $\beta(1)\beta(2)$, and $[\alpha(1)\beta(2) + \beta(1)\alpha(2)]/\sqrt{2}$), the singlet and triplet form in a 1:3 ratio. The two states are initially degenerate in energy. The PESs for both states remain flat, indicating weak long-range interactions. The PESs become attractive starting at r[9MOG–N] = 6 Å and reach a potential well at 4.70 Å, where the $^{\bullet}$NO moiety moves over 9MOG$^{\bullet+}$, forming an electrostatic ″encounter″ complex (point ① in Figure 3a). The encounter can be considered a mixture of $^{1,\mathrm{OS}}$encounter and ^{3}encounter.

The two of them diverge at point ② ([9MOG–N] = 4.13 Å), where the open-shell singlet drops in energy below the triplet. Along the triplet surface, a weakly bound ^{3}precursor forms at point ③ (r[9MOG–N] = 3.09 Å) with a binding energy of 0.15 eV. The presence of a structurally flexible precursor complex is crucial, as it allows repeated encounters between reactants, enabling them to explore different orientations and increasing the probability of forming a reactive configuration. Toward shorter intermolecular distances, the triplet becomes repulsive.

For the singlet pathway, point ② represents a barrier for interconversion from $^{1,\mathrm{OS}}$encounter to a $^{1,\mathrm{OS}}$precursor located at point ④ (r[9MOG–N] = 2.77 Å) with binding energy of 0.33 eV. As the distance further decreases, the open-shell singlet increases in energy and reaches a conical intersection at point ⑤ (r[9MOG–N] = 2.59 Å), where it becomes energetically degenerate with a closed-shell singlet, facilitating internal conversion. The open-shell singlet terminates abruptly at 2.3 Å, reflecting the difficulty in converging the open-shell wave function at short intermolecular distances. Internal conversion leads to the global minimum at point ⑥ (r[9MOG–N] = 2.386 Å), where a covalent $^{1,\mathrm{CS}}$[5-NO-9MOG]$^{+}$ forms.

Figure 3b – d illustrates the evolution of NO bond length, spin density, and charge throughout the reaction. On the triple surface, spin and charge remain localized on the 9MOG moiety, while NO retains a neutral character, except for minor charge transfer at r[9MOG–N] = 4 – 6 Å, corresponding to the formation of the ^{3}encounter complex. In the open-shell singlet state, the NO bond length, charge, and spin remain nearly identical to the triplet case until the divergence point ②, beyond which NO begins to lose spin density, accompanied by a gradual increase in positive charge. The abrupt changes in NO spin and charge at r[9MOG–N] = 2.77 Å, along with the elongation of rNO, indicate substantial charge transfer and structural reorganization upon internal conversion. Collectively, these changes highlight key events from the initial encounter to the formation of distinct complexes.

2) Nitrosation at short range. The closed-shell singlet is the energetically most favorable at short distances. Both open-shell singlet and triplet may funnel their populations to this state. Therefore, it is informative to explore the evolution of the closed-shell singlet over a wider range of r[9MOG–N], as shown in Figure 4a. The formation of ^{1,CS}[5-NO-9MOG]$^+$ at r[9MOG–N] = 2.386 Å (see the inset of Figure 4b) represents the most significant contribution to the nitration process. As shown in Figure 4b – c, rNO of ^{1,CS}[5-NO-9MOG]$^+$ stretches to 1.15 Å, meanwhile its rN–C5 shortens to 1.6 Å, indicating a strong shift of N electron bonding toward the C5 site. The positive charge in ^{1,CS}[5-NO-9MOG]$^+$ is uniformly distributed across the complex, as illustrated by the electrostatic potential (ESP)-fitted charge distribution, with δ^+(NO) of 0.15.

The ^{1,CS}[5-NO-9MOG]$^+$ may interconvert into a loosely bound ion-dipole complex at r[9MOG–N] = 3.98 Å, referred to as ^{1,CS}CT. This interconversion is mediated by a low-energy TS located at r[9MOG–NO] = 3.23 Å. In ^{1,CS}CT, δ^+(NO) increases to 0.43 and rNO decreases to 1.12 Å. This complex is mechanistically significant as it directly connects to the CT product asymptotic limit, 9MOG + NO$^+$. Notably, separation of ^{1}CT into 9MOG + NO$^+$ occurs without reverse activation barriers, and the changes in NO spin and charge are continuous throughout the process.

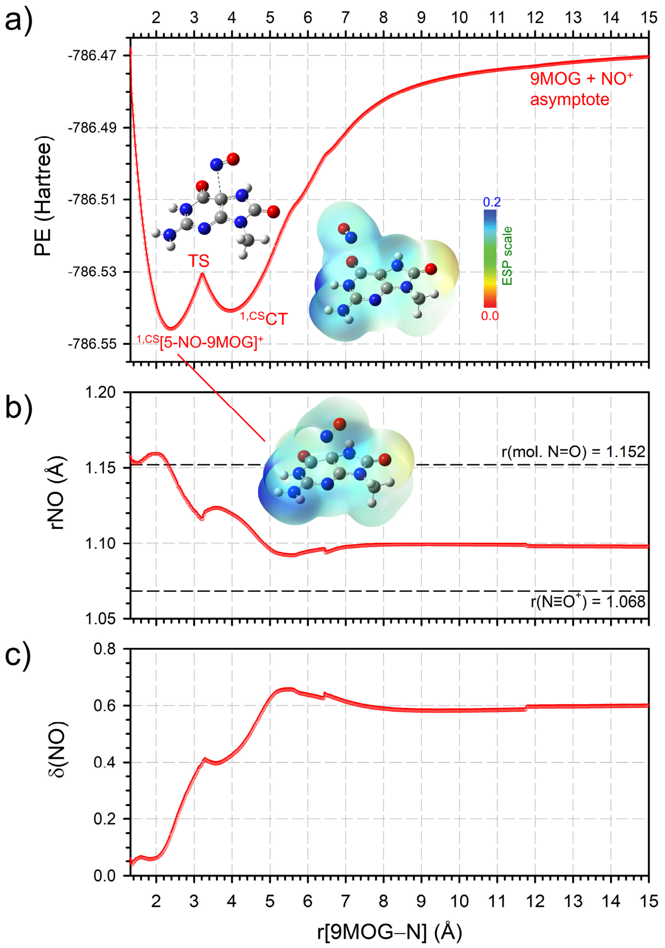

Figure 4. Closed-shell singlet PES for $9MOG^{\bullet+}$ + $^{\bullet}NO$ along r[9MOG−N], the distance between the center-of-mass of $9MOG^{\bullet+}$ and the N-terminal of $^{\bullet}NO$, calculated at the ωB97XD/6-31+G(d,p) level. a) Changes in reaction potential energy; and b–c) variations in NO bond length and NBO charge. The PES illustrates the formation of a covalent complex at short range and charge transfer at long range. Insets show structures for ^{1,CS}[5-NO-9MOG]$^{+}$, ^{1}CT, and the associated TS (C: gray; H: white; N: blue; and O: red). Complex structures feature electrostatic potential (ESP, in eV)-fitted charge distribution.

B. Spin-orbit coupling and charge transfer

Following Figure 4, a possible pathway for CT could be $^{1,OS}[9MOG^{\bullet+}(\uparrow)\cdots(\downarrow)^{\bullet}NO] \rightarrow {}^{1,CS}CT \rightarrow$ 9MOG + $^{+}$NO. Nevertheless, this pathway requires the formation of electrostatic and covalent complexes at high E_{CM} (> 2 eV), where the formation efficiency and lifetime for these complexes are actually suppressed. Alternatively, a triplet-mediated CT pathway may be considered. To this end, we need to evaluate the potential for ISC from triplet reactants to closed-shell singlet products. Previously, we proposed a spin-orbit charge transfer (SOCT) mechanism for $9MG^{\bullet+}$ + $^{\bullet}NO$ based on the analysis of frontier molecular orbitals.[17] In that system, the ^{3}precursor complex corresponds to $^{3}[9MG^{\bullet+}(\uparrow)\cdots(\uparrow)^{\bullet}NO]$, while the ^{1}CT complex correlates with $^{1,\mathrm{CS}}[9\mathrm{MG}(\uparrow\downarrow)\cdots\mathrm{NO}^{+}]$. During ISC, the electron in the triplet SOMO (predominantly π* on NO) transfers into SOMO – 1 (predominantly π* on $9\mathrm{MG}^{\bullet+}$) while rephasing spin. The orbital angular momentum change between orthogonal π*(NO) and π*($9\mathrm{MG}^{\bullet+}$) is compensated by the electron spin angular momentum shift, conserving total angular momentum. Following ISC, the system proceeds along the ^{1}CT complex toward 9MG + NO^{+}. Throughout this process, rNO remains at the neutral bond length, resulting in vibrational excitation in NO^{+}. This vibrational excitation serves as a dynamics signature for SOCT.

Given the similarities in electron configurations and PES profiles for $^{\bullet}$NO with $9\mathrm{MG}^{\bullet+}$ and $9\mathrm{MOG}^{\bullet+}$, as well as the vibrational excitation detected in NO^{+} product ions, the SOCT mechanism is likely applicable to $9\mathrm{MOG}^{\bullet+}$ + $^{\bullet}$NO. A key factor is that a triplet radical-ion pair is often exceptionally long-lived, with lifetimes extending up to 200 – 600 μs.[86-89] This is consistent with the large n value used in the LOC fitting of the CT cross section of $9\mathrm{MOG}^{\bullet+}$ + $^{\bullet}$NO, which implies the formation of a long-lived complex.

To verify the SOCT of $9\mathrm{MOG}^{\bullet+}$ + $^{\bullet}$NO, we first estimated the reactant separation at which the SOCT would likely occur. We assumed that the excitation energy required for the transition from the triplet to the closed-shell singlet (ΔE_{TS}) could be provided by the increased ion-dipole interaction during the transition of $[9\mathrm{MOG}^{\bullet+}(\uparrow)\cdots(\uparrow)^{\bullet}\mathrm{NO}] \rightarrow [9\mathrm{MOG}\ (\uparrow\downarrow)\cdots{}^{+}\mathrm{NO}]$. The dipole moment ($\mu_D$) and polarizability ($\alpha$) of the neural reactant were obtained from ωB97XD/6-31+G(d,p) calculations. Ion-dipole interaction was estimated using $V(r) = -\alpha q^2/2r^4 - Cq\mu_D/r^2$,[82] where q is the ion charge, r denotes the center-of-mass reactant distance, and C is the dipole locking constant (0.386). Based on this calculation, SOCT is expected to occur at $r \leq 5$ Å with $\Delta E_{\mathrm{TS}} \leq 0.35$ eV. To assess whether spin-orbit coupling is sufficiently strong in this region, the SOCC between triplet and closed-shell singlet was evaluated using the TDDFT/TDA approach.[76] The one-electron and mean-field SOCC values are 74 and 44 cm^{-1}, respectively — sufficient for ISC in a conjugated system. The SOCC decreases as the reactants move apart and ΔE_{TS} increases. The one-electron SOCC drops below 11 cm^{-1} when ΔE_{TS} exceeds 1 eV, indicating a diminishing ISC probability at larger separations.

C. Nitrosation structures and energetics

Following spin dynamics and PESs, we computed all possible nitrosation structures. The results are presented in Schemes 3 and 4, with Cartesian coordinates for the reaction structures provided in the Supplementary Material. Scheme 3 outlines three nitrosation pathways in the singlet state: barrierless N-terminal addition at C5, forming ^{1,CS}[5-NO-9MOG]$^+$ (which exists in *syn*- and *anti*-conformations relative to the imidazole ring); N-terminal addition at N2, resulting in ^{1,CS}[2-NHNO-3H-9MOG]$^+$, which is accompanied by proton transfer from N2 to N3; and synchronous cycloaddition to ^{1,OS}[2,4-ṄO-9MOĠ]$^+$. Additionally, ^{1,CS}[5-NO-9MOG]$^+$ may interconvert to ^{1,CS}[3-NO-9MOG]$^+$. No O-terminal addition was identified in the singlet.

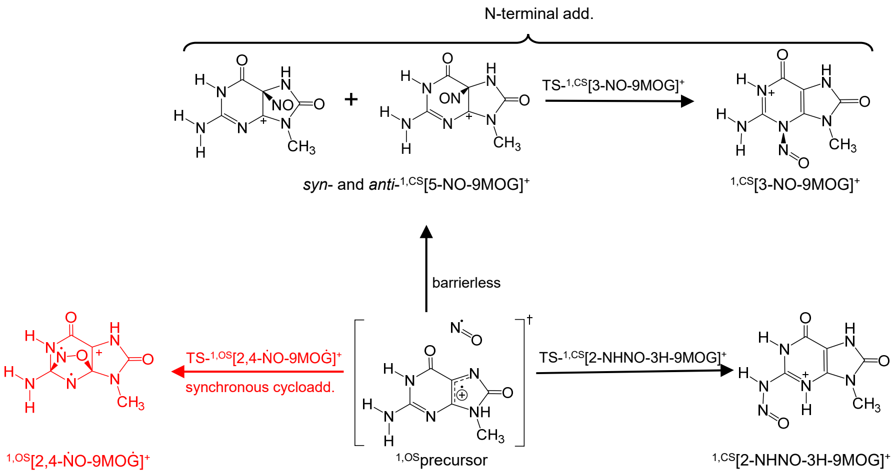

Scheme 3. Nitrosation pathways and products of $9MOG^{\bullet+}$ in the singlet state.

The triplet state exhibits a broad range of nitrosation pathways. The top portion of Scheme 4 illustrates N- and O-terminal $^{\bullet}$NO-addition to $9MOG^{\bullet+}$. Notably, the formation of ^{3}[8-ON-9MOG]$^+$ and ^{3}[8-NO-9MOG]$^+$ leads to the cleavage of the imidazole ring at the N7–C8 bond. The bottom portion of Scheme 4 highlights cycloadduct formation. The formation of ^{3}[2,4-NO-9MOG]$^+$ occurs in an asynchronously concerted manner, whereas the 7,8-ON-cycloaddition proceeds sequentially via the ^{3}[8-NO-9MOG]$^+$ intermediate. The 7,8-NO-cycloaddition can occur through either a synchronous concerted or sequential mechanism. Similar to the 8-addition, both 7,8-NO and 7,8-ON-cycloaddition lead to imidazole ring cleavage, expanding it into a seven-membered macrocycle (structures **1** and **2** in Scheme 4).

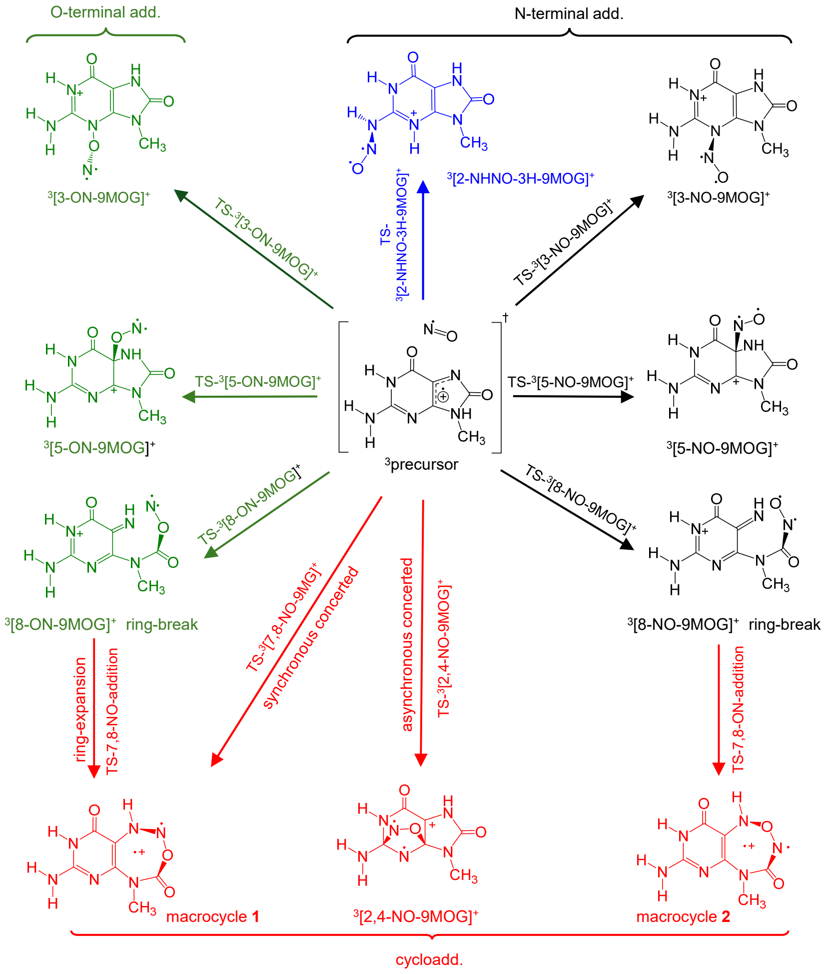

Scheme 4. Nitrosation pathways and products of $9MOG^{\bullet+}$ in the triplet state.

In singlet biradicals, two unpaired electrons remain separately on 9MOG and NO. In triplet N-terminal adducts, the unpaired electron of $9MOG^{\bullet+}$ shifts to the oxygen of NO. In triplet O-terminal adducts, the unpaired electron of $9MOG^{\bullet+}$ shifts to the nitrogen of NO, resulting in both unpaired electrons being localized at the N-terminal. In triplet cycloadducts, two unpaired electrons are equally distributed between $9MOG^{\bullet+}$ and $^{\bullet}$NO. In all adducts, positive charge remains predominantly on 9MOG.

Table 1 compares nitrosation product ΔHs and activation barriers, calculated at different levels of theory. All three theoretical methods predict ^{1,CS}[5-NO-9MOG]$^+$ as the only exothermic nitrosation pathway without a reverse barrier, consistent with the PES result. All other singlet and triplet products are endothermic and require high activation barriers. According to CASPT2 calculations, the threshold energy for these pathways ranges from 1.36 to 3.98 eV, except for ^{1,CS}[3-NO-9MG]$^+$, which has an endothermicity of 0.24 eV and a barrier of 0.32 eV. However, the absence of an endothermic nitrosation product in the experiment indicates that this product channel does not happen.

Table 1. Reaction ΔH (298 K, eV) calculated at different levels of theory

Species	ωB97XD/6-31+G(d,p)[a]	DLPNO-CCSD(T)/aug-cc-pVTZ	CASPT2/ANO-L-VTZP
^{1,CS}[2-NHNO-3H-9MOG]$^+$	-0.27 (1.90)[b]	0.25 (2.20)	0.00 (1.86)
^{1,CS}[3-NO-9MOG]$^+$	0.02 (0.24)	0.47 (0.54)	0.24 (0.32)
^{1,CS}[5-NO-9MOG]$^+$	-0.77/-0.69 (-*syn*/-*anti*) (-0.61)[c]	-0.42/-0.32 (-*syn*/-*anti*) (-0.23)[c]	-0.55/-0.45 (-*syn*/-*anti*) (-0.35)[c]
^{1,OS}precursor	-0.92^{AP}	—	—
^{1,OS}[2,4-$\dot{N}$O-9MO$\dot{G}$]$^+$	2.92^{AP} (2.93)^{AP}	—	—
^{3}precursor	-0.58	-0.12	-0.14
^{3}[2NHNO-3H-9MOG]$^+$	1.55 (3.60)	2.35 (4.28)	2.03 (3.98)
^{3}[3-NO-9MOG]$^+$	1.57 (1.61)	2.38 (2.66)	2.03 (2.05)
^{3}[5-NO-9MOG]$^+$	0.18 (0.27)	0.82 (0.85)	0.59 (0.68)
^{3}[8-NO-9MOG]$^+$	1.33 (1.86)	1.87 (2.47)	1.77 (2.24)
^{3}[3-ON-9MOG]$^+$	2.80 (2.89)	3.41 (3.45)	3.18 (3.23)
^{3}[5-ON-9MOG]$^+$	0.79 (0.89)	1.32 (1.46)	1.24 (1.36)
^{3}[8-ON-9MOG]$^+$	1.98 (2.40)	2.37 (2.84)	2.42 (2.74)
^{3}[2,4-NO-9MOG]$^+$	3.08 (3.21)	3.55 (3.72)	3.56 (3.64)
7-member macrocyclic 1	1.50 (2.73 from precursor, 2.40 from [8-ON-9MOG]$^+$)	2.21 (3.32 from precursor, 2.96 from [8-ON-9MOG]$^+$)	2.14 (3.00 from precursor, 2.86 from [8-ON-9MOG]$^+$)
7-member macrocyclic 2	2.46 (2.56 from [8-NO-9MOG]$^+$)	3.19 (3.21 from [8-NO-9MOG]$^+$)	3.08 (3.10 from [8-NO-9MOG]$^+$)

[a] DFT energy of $^{\bullet}$NO was calculated by subtracting experimental AIE($^{\bullet}$NO) from the energy of NO$^+$, and spin purification was applied to singlet biradicals (indicated by superscript AP);

[b] Numbers in parentheses indicate barriers for corresponding transition states.

[c] The barrier refers to isomerization between *syn*- and *anti*-^{1,CS}[5-NO-9MOG]$^+$.

Compared to CASPT2, ωB97XD underestimates reaction energies by 0.2 – 0.4 eV, whereas DLPNO-CCSD(T) overestimates energies by 0.1 – 0.4 eV. The experiment confirmed that nitrosation is sufficiently exothermic to induce water ligand elimination. The water-elimination energy for probable 9MOG$^{\bullet+}\cdot$H$_2$O structures ranges from 0.58 to 0.68 eV, so the nitrosation ΔH (298 K) should be comparable to this energy. Consequently, both CASPT2 and spin-projected DFT predict reasonable reaction energetics, *i.e.*, -0.77 /-0.69 eV for *syn/anti*-^{1,CS}[5-NO-9MOG]$^+$ at ωB97XD vs. -0.55 / -0.45 eV at CASPT2.

The $\langle \hat{S}^2 \rangle$ and T1 diagnostics for individual structures are enumerated in the Supplementary Table S1, along with a comparison of energy differences between different levels. For closed-shell singlet structures, $T1$ remains ≤ 0.016; while for triplet structures, $\langle \hat{S}^2 \rangle$ remains at 2.00 and $T1$ remains < 0.023, indicating minimal, if any, spin contamination. However, the $\langle \hat{S}^2 \rangle$ for ^{1,OS}precursor and ^{1,OS}[2,4-$\dot{N}$O-9MO$\dot{G}$]$^+$ ranges from 0.66 to 0.92, suggesting their strong multi-configuration characters and warranting spin purification and multireferential treatment.

D. Anisotropic PES leads to stereodynamics control and low reaction efficiency

Besides the common SOCT pathway, it is instructive to compare the nitrosation behavior of 9MOG$^{\bullet+}$ vs. 9MG$^{\bullet+}$. The reaction of 9MG$^{\bullet+}$ + $^{\bullet}$NO produced ^{1,CS}[7-NO-9MG]$^+$ as the major product with ΔH (298 K) = -1.20 eV and no reverse barrier and ^{3}[8-NO-9MG]$^+$ as the minor product with ΔH (298 K) = 0.45 eV and activation barrier = 0.62 eV.[18] The nitrosation reaction efficiency for 9MG$^{\bullet+}$ is 0.54% at E_{CM} = 0.05 eV and 0.5% at 0.1 eV. In comparison, the nitrosation of 9MOG$^{\bullet+}$ produced only exothermic ^{1,CS}[5-NO-9MOG]$^+$ with ΔH (298 K) = -0.45 – -0.55 eV and no reverse barrier and an efficiency of no more than 0.3% at E_{CM} ≤ 0.1 eV.

The low nitrosation yield for 9MOG$^{\bullet+}$ (and 9MG$^{\bullet+}$) warrants further analysis. A common feature of the nitrosative reaction of nucleobase radical cations is their spin selectivity. As aforementioned, radical-radical collisions distribute between singlet and triplet in a 1:3 ratio. Since triplet nitrosation pathways are entirely endothermic, the exothermic pathway is unequivocally associated with the singlet, placing the expected maximum reaction efficiency at 25%. However, this assumption holds only if ^{1,OS}encounter and ^{1,OS}precursor can form effectively in the collisions and all ultimately form a closed-shell singlet state.

This prompted us to examine the formation efficiency of ^{1,OS}encounter and ^{1,OS}precursor. Both complexes are weakly bound through electrostatic interaction, making them ineffective at trapping collision partners. Consequently, a large fraction of collisions likely result in non-reactive scattering. Additionally, anisotropic PES and the resulting stereodynamics influence collision outcomes. Figure 5 compares the two singlet PESs for $^{\bullet}$NO attacking 9MOG$^{\bullet+}$ at the N- vs. O-terminal. Each PES is plotted as a function of the distance between the center-of-mass of 9MOG and the projectile atom of $^{\bullet}$NO. Compared to the N-first collision, the O-first collision exhibits two distinct features: 1) the surface is flatter at large distances yet more repulsive at short distances. The absence of an appreciable attractive potential well renders the collision energetically unfavorable; and 2) the collision remains in ^{1,OS}[9MOG$^{\bullet+}$(↑)···ON$^{\bullet}$(↓)] and lacks conical intersection for internal conversion to a closed-shell singlet, ultimately leading to non-reactive scattering. The non-reactivity is further supported by the minimal changes in bond length, charge, and spin of NO during the O-first collision, as shown in Supplementary Figure S2. As a result, only the N-first orientation facilitates the nitrosation of 9MOG$^{\bullet+}$.

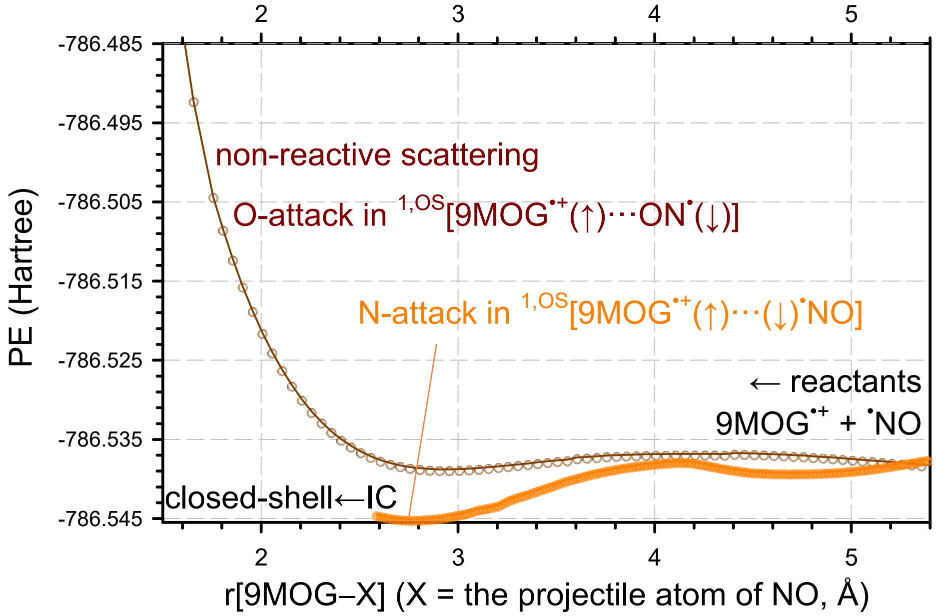

Figure 5. Singlet PES for the $^{\bullet}$NO collision with 9MOG$^{\bullet+}$ at different orientations, calculated at AP-ωB97XD/6-31+G(d,p).

Using the Rice-Ramsperger-Kessel-Marcus (RRKM) theory,[90] we also calculated rate constants (*k*) for ^{1,OS}precursor complex′s nitrosation reaction *vs*. decay back to reactants 9MOG$^{\bullet+}$ + NO^{+}. The *k* values were calculated using Zhu and Hase′s code,[91] with density of states evaluated via a direct count algorithm.[92] Since no reverse barrier exists, orbit transition states[93] were assumed with the reaction orbital angular momentum given by $L = \mu \cdot v \cdot \sqrt{\sigma_{collision}/\pi}$, where μ is the reduced mass, and v is the relative velocity of the collision partners. The calculations revealed that once ^{1,OS}precursor has formed, it can effectively proceed toward nitrosation with the branching ratio for decay back into reactants of < 0.1%. The RRKM analysis has reinforced that stereodynamics is the rate-limiting factor.

The anisotropic PES also affects collisions in the triplet. As shown in the Supplementary Figure S3, the O-first triplet collision produces shallower potential wells for ^{3}encounter and ^{3}precursor compared to the N-first collision. Moreover, stereodynamics influences spin-orbit charge transfer, as the O-terminal complexes exhibit weaker spin-orbit coupling than the N-terminal complexes at the same reactant distance. This finding aligns with the large *n* value required for the LOC fitting of the CT cross section in Figure 1B. Notably, anisotropic PES and stereodynamics are common in the reactions of $^•$NO.[94] The intuitive interpretation of stereodynamics is often based on the analysis of the molecular environment (*e.g.*, steric hindrance). In the present case, however, the dynamical origin of stereodynamics control is attributed to the different intrinsic reactivities at the two terminus of $^•$NO. A similar observation was reported in the bimolecular nucleophilic substitution (S_N2) reaction of F^- + $(CH_3)_3CI$, where the competition between substitution and elimination pathways — rather than the steric hindrance from the bulky methylated alkyl halide — acts as the primary factor governing the intrinsic reaction branching.[95]

V. Conclusions

A guided-ion beam mass spectrometry investigation was conducted to analyze the interactions between $9MOG^{•+}$ and $^•$NO. The propensities and accessibilities of various reaction pathways are strongly influenced by electron configurations, reaction energies, and collision orientations. The biradical collisions produced two precursor complexes, $^{1,OS}[9MOG^{•+}(\uparrow)\cdots(\downarrow)^•NO]$ and $^3[9MOG^{•+}(\uparrow)\cdots(\uparrow)^•NO]$, in a 1:3 ratio. The open-shell singlet complex underwent internal conversion, yielding exothermic product $^{1,CS}[5\text{-}NO\text{-}9MOG]^+$ at low energies. In contrast, the triple complex facilitated spin-orbit charge transfer at high energies, imprinting vibrational excitation into product ions, $NO^+(v^+ = 1)$. The low reaction yield is attributed to spin selectivity and anisotropic PES that govern the $^{\bullet}$NO collision dynamics with 9MOG$^{\bullet+}$. Stereodynamics restricted the reaction to nitric oxide N-terminal collisions with 9MOG$^{\bullet+}$, whereas O-oriented collisions resulted in non-reactive scattering. This study provides key insights into radical-pair dynamics and $^{\bullet}$NO-mediated DNA damage. The findings are biologically relevant in contexts where $^{\bullet}$NO serves as a potent nitrosation agent and an intrinsic radiosensitizer *in vivo* to enhance cancer radiotherapy (at low-radiation doses). The charge transfer between OG$^{\bullet+}$ and $^{\bullet}$NO may serve as a mechanism to modulate radical scavenging in hypoxic tumor microenvironments. Although the reaction is endothermic and involves vibrational excitation of the NO product — making it energetically demanding — it may still proceed when coupled to exothermic enzymatic or catalyzed processes within a complex reaction network, or when supported by external energy sources such as ionizing radiation or photodynamic therapy. The low nitrosation efficiency of G$^{\bullet+}$ and OG$^{\bullet+}$ is somewhat unexpected. This suggests that radiosensitization by $^{\bullet}$NO may involve other pathways in addition to G$^{\bullet+}$/OG$^{\bullet+}$–$^{\bullet}$NO combination, such as the conversion of $^{\bullet}$NO to NO$_X$ species which can then nitrate or oxidize nucleobase radicals. The present work provides an entry point to mechanistic studies of NO$_X$-associated lesions. We are currently investigating the reactions of $^{\bullet}$NO$_2$ with G$^{\bullet+}$ and OG$^{\bullet+}$, which may offer further insights.

VI. Supplementary Material

The supplementary material includes additional PESs, spin and T1 diagnostics, and cartesian coordinates for reaction structures.

VII. Acknowledgements

This work was supported by the National Science Foundation (Grant No. CHE 2350109). Benny acknowledges the CUNY Graduate Center Dissertation Fellowship. The authors are grateful to Dr. Toru Saito (Hiroshima City University) for his valuable insights on the application of spin projection.

VIII. Data Availability Statement

The data that support the findings of this study are available within the article and its supplementary material.

References

[1] X. Garcia and F. Stein,"Nitric oxide," Semin. Pediatr. Infect. Dis. **17**, 55-57 (2006).
[2] H. Terato, A. Masaoka, K. Asagoshi, A. Honsho, Y. Ohyama, T. Suzuki, M. Yamada, K. Makino, K. Yamamoto, and H. Ide,"Novel repair activities of AlkA (3-methyladenine DNA glycosylase II) and endonuclease VIII for xanthine and oxanine, guanine lesions induced by nitric oxide and nitrous acid," Nucleic Acids Res. **30**, 4975-4984 (2002).
[3] D. A. Wink, K. S. Kasprzak, C. M. Maragos, R. K. Elespuru, M. Misra, T. M. Dunams, T. A. Cebula, W. H. Koch, A. W. Andrews, J. S. Allen, and L. K. Keefer,"DNA deaminating ability and genotoxicity on nitric oxide and its progenitors," Science **254**, 1001-1003 (1991).
[4] S. Tamir, S. Burney, and S. R. Tannenbaum,"DNA damage by nitric oxide," Chem. Res. Toxicol. **9**, 821-827 (1996).
[5] T. Nguyen, D. Brunson, C. L. Crespi, B. W. Penman, J. S. Wishnok, and S. R. Tannenbaum,"DNA damage and mutation in human cells exposed to nitric oxide in vitro," Proc. Natl. Acad. Sci. U. S. A. **89**, 3030-3034 (1992).
[6] S. Kawanishi, S. Ohnishi, N. Ma, Y. Hiraku, S. Oikawa, and M. Murata,"Nitrative and oxidative DNA damage in infection-related carcinogenesis in relation to cancer stem cells," Genes Environ. **38**, 26 (2017).
[7] P. Howard-Flanders,"Effect of nitric oxide on the radiosensitivity of bacteria," Nature **180**, 1191-1192 (1957).
[8] L. H. Gray, F. O. Green, and C. A. Hawes,"The effect of nitric oxide on the radiosensitivity of tumor cells," Nature **182**, 952-953 (1958).
[9] J. B. Mitchell, D. A. Wink, W. DeGraff, J. Gamson, L. K. Keefer, and M. C. Krishna,"Hypoxic mammalian cell radiosensitization by nitric oxide," Cancer Res. **53**, 5845-5848 (1993).
[10] P. Wardman, K. Rothkamm, L. K. Folkes, M. Woodcock, and P. J. Johnston,"Radiosensitization by nitric oxide at low radiation doses," Radiat. Res. **167**, 475-484 (2007).
[11] G. D. Stewart, J. Nanda, E. Katz, K. J. Bowman, J. G. Christie, D. J. G. Brown, D. B. McLaren, A. C. P. Riddick, J. A. Ross, G. D. D. Jones, and F. K. Habib,"DNA strand breaks and hypoxia response inhibition mediate the radiosensitisation effect of nitric oxide donors on prostate cancer under varying oxygen conditions," Biochem. Pharmacol. **81**, 203-210 (2011).
[12] L. K. Folkes and P. O'Neill,"DNA damage induced by nitric oxide during ionizing radiation is enhanced at replication," Nitric Oxide **34**, 47-55 (2013).
[13] L. K. Folkes and P. O'Neill,"Modification of DNA damage mechanisms by nitric oxide during ionizing radiation," Free Radic. Biol. Med. **58**, 14-25 (2013).
[14] J. Zhou, O. Kostko, C. Nicolas, X. Tang, L. Belau, M. S. de Vries, and M. Ahmed,"Experimental observation of guanine tautomers with VUV photoionization," J. Phys. Chem. A **113**, 4829-4832 (2009).
[15] C. E. Crespo-Hernández, R. Arce, Y. Ishikawa, L. Gorb, J. Leszczynski, and D. M. Close,"Ab initio ionization energy thresholds of DNA and rna bases in gas phase and in aqueous solution," J. Phys. Chem. A **108**, 6373-6377 (2004).
[16] S. Steenken and S. V. Jovanovic,"How easily oxidizable is DNA? One-electron reduction potentials of adenosine and guanosine radicals in aqueous solution," J. Am. Chem. Soc. **119**, 617-618 (1997).
[17] J. Benny and J. Liu,"Spin-orbit charge transfer from guanine and 9-methylguanine radical cations to nitric oxide radicals and the induced triplet-to-singlet intersystem crossing," J. Chem. Phys. **159**, 085102 (2023).
[18] J. Benny, T. Saito, and J. Liu,"Nitrosation mechanisms, kinetics, and dynamics of the guanine and 9-methylguanine radical cations by nitric oxide — radical–radical combination at different electron configurations," J. Chem. Phys. **161**, 125101 (2024).
[19] P. M. Cullis, M. E. Malone, and L. A. Merson-Davies,"Guanine radical cations are precursors of 7,8-dihydro-8-oxo-2'-deoxyguanosine but are not precursors of immediate strand breaks in DNA," J. Am. Chem. Soc. **118**, 2775-2781 (1996).
[20] J. Cadet, T. Douki, D. Gasparutto, and J.-L. Ravanat,"Oxidative damage to DNA: Formation, measurement and biochemical features," Mutation Res. **531**, 5-23 (2003).
[21] A. M. Fleming and C. J. Burrows,"8-oxo-7,8-dihydroguanine, friend and foe: Epigenetic-like regulator versus initiator of mutagenesis," DNA Repair **56**, 75-83 (2017).
[22] S. D. Bruner, D. P. G. Norman, and G. L. Verdine,"Structural basis for recognition and repair of the endogenous mutagen 8-oxoguanine in DNA," Nature **403**, 859-866 (2000).
[23] R. P. Hickerson, C. L. Chepanoske, S. D. Williams, S. S. David, and C. J. Burrows,"Mechanism-based DNA−protein cross-linking of MutY via oxidation of 8-oxoguanosine," J. Am. Chem. Soc. **121**, 9901-9902 (1999).

[24] D. C. Malins, N. L. Polissar, G. K. Ostrander, and M. A. Vinson,"Single 8-oxo-guanine and 8-oxo-adenine lesions induced marked changes in the backbone structure of a 25-base DNA strand," Proc. Natl. Acad. Sci. U. S. A. **97**, 12442-12445 (2000).

[25] J. Zhang, G. Perry, M. A. Smith, D. Robertson, S. J. Olson, D. G. Graham, and T. J. Montine,"Parkinson's disease is associated with oxidative damage to cytoplasmic DNA and RNA in substantia nigra neurons," Am. J. Pathol. **154**, 1423-1429 (1999).

[26] M. A. Lovell and W. R. Markesbery,"Ratio of 8-hydroxyguanine in intact DNA to free 8-hydroxyguanine is increased in Alzheimer disease ventricular cerebrospinal fluid," Arch. Neurol. **58**, 392-396 (2001).

[27] H. Sies, *Oxidative stress* (Academic Press, London, UK, 1985), p. 507.

[28] S. Steenken, S. V. Jovanovic, M. Bietti, and K. Bernhard,"The trap depth (in DNA) of 8-oxo-7,8-dihydro-2'-deoxyguanosine as derived from electron-transfer equilibria in aqueous solution," J. Am. Chem. Soc. **122**, 2373-2374 (2000).

[29] V. Palivec, E. Pluhařová, I. Unger, B. Winter, and P. Jungwirth,"DNA lesion can facilitate base ionization: Vertical ionization energies of aqueous 8-oxoguanine and its nucleoside and nucleotide," J. Phys. Chem. B **118**, 13833-13837 (2014).

[30] P. Diamantis, I. Tavernelli, and U. Rothlisberger,"Redox properties of native and damaged DNA from mixed quantum mechanical/molecular mechanics molecular dynamics simulations," J. Chem. Theory Comput. **16**, 6690-6701 (2020).

[31] R. K. O. Sigel, E. Freisinger, and B. Lippert,"Effects of N7-methylation, N7-platination, and C8-hydroxylation of guanine on H-bond formation with cytosine: Platinum coordination strengthens the Watson-Crick pair," JBIC, J. Biol. Inorg. Chem. **5**, 287-299 (2000).

[32] Y. Fang and J. Liu,"Reaction of protonated tyrosine with electronically excited singlet molecular oxygen ($a^1\Delta_g$): An experimental and trajectory study," J. Phys. Chem. A **113**, 11250-11261 (2009).

[33] L. Feketeová, E. Yuriev, J. D. Orbell, G. N. Khairallah, and R. A. J. O'Hair,"Gas-phase formation and reactions of radical cations of guanosine, deoxyguanosine and their homodimers and heterodimers," Int. J. Mass Spectrom. **304**, 74-82 (2011).

[34] P. Cheng and D. K. Bohme,"Gas-phase formation of radical cations of monomers and dimers of guanosine by collision-induced dissociation of Cu(II)-guanosine complexes," J. Phys. Chem. B **111**, 11075-11082 (2007).

[35] A. Dang, Y. Liu, and F. Tureček,"Uv-vis action spectroscopy of guanine, 9-methylguanine, and guanosine cation radicals in the gas phase," J. Phys. Chem. A **123**, 3272-3284 (2019).

[36] Y. Sun, M. Tsai, M. M. Moe, and J. Liu,"Dynamics and multiconfiguration potential energy surface for the singlet O_2 reactions with radical cations of guanine, 9-methylguanine, 2'-deoxyguanosine, and guanosine," J. Phys. Chem. A **125**, 1564-1576 (2021).

[37] M. M. Moe, M. Tsai, and J. Liu,"Singlet oxygen oxidation of the radical cations of 8-oxo-2'-deoxyguanosine and its 9-methyl analogue: Dynamics, potential energy surface, and products mediated by C5-O_2-addition," ChemPlusChem **86**, 1243-1254 (2021).

[38] A. N. Krutchinsky, I. V. Chernushevich, V. L. Spicer, W. Ens, and K. G. Standing,"Collisional damping interface for an electrospray ionization time-of-flight mass spectrometer," J. Am. Soc. Mass Spectrom. **9**, 569-579 (1998).

[39] P. B. Armentrout,"Kinetic energy dependence of ion-molecule reactions: Guided ion beams and threshold measurement," Int. J. Mass Spectrom. **200**, 219-241 (2000).

[40] C. Rebick and R. D. Levine,"Collision induced dissociation: A statistical theory," J. Chem. Phys. **58**, 3942-3952 (1973).

[41] W. J. Chesnavich and M. T. Bowers,"Theory of translationally driven reactions," J. Phys. Chem. **83**, 900-905 (1979).

[42] R. D. Levine and R. B. Bernstein, *Molecular reaction dynamics and chemical reactivity* (Oxford University Press, New York, 1987),

[43] J. Liu, B. van Devener, and S. L. Anderson,"Collision-induced dissociation of formaldehyde cations: The effects of vibrational mode, collision energy, and impact parameter," J. Chem. Phys. **116**, 5530-5543 (2002).

[44] P. J. Chantry,"Doppler broadening in beam experiments," J. Chem. Phys. **55**, 2746-2759 (1971).

[45] C. Lifshitz,"Kinetic shifts," Eur. J. Mass Spectrom. **8**, 85-98 (2002).

[46] Y. Sun, M. M. Moe, and J. Liu,"Mass spectrometry and computational study of collision-induced dissociation of 9-methylguanine-1-methylcytosine base-pair radical cation: Intra-base-pair proton transfer and hydrogen transfer, non-statistical dissociation, and reaction with a water ligand," Phys. Chem. Chem. Phys. **22**, 14875-14888 (2020).

[47] M. B. Sowa-Resat, P. A. Hintz, and S. L. Anderson,"Dissociation energies for small carbon cluster ions (C_{2-19}^+) measured by collision-induced dissociation," J. Phys. Chem. **99**, 10736-10741 (1995).

[48] M. J. Frisch, G. W. Trucks, H. B. Schlegel, G. E. Scuseria, M. A. Robb, J. R. Cheeseman, G. Scalmani, V. Barone, G. A. Petersson, H. Nakatsuji, X. Li, M. Caricato, A. V. Marenich, J. Bloino, B. G. Janesko, R. Gomperts, B. Mennucci, H. P. Hratchian, J. V. Ortiz, A. F. Izmaylov, J. L. Sonnenberg, D. Williams-Young, F. Ding, F. Lipparini, F. Egidi, J. Goings, B. Peng, A. Petrone, T. Henderson, D. Ranasinghe, V. G. Zakrzewski, J. Gao, N. Rega, G. Zheng, W. Liang, M. Hada, M. Ehara, K. Toyota, R. Fukuda, J. Hasegawa, M. Ishida, T. Nakajima, Y. Honda, O. Kitao, H. Nakai, T. Vreven, K. Throssell, J. A. Montgomery Jr., J. E. Peralta, F. Ogliaro, M. J. Bearpark, J. J. Heyd, E. N. Brothers, K. N. Kudin, V. N. Staroverov, T. A. Keith, R. Kobayashi, J. Normand, K. Raghavachari, A. P. Rendell, J. C. Burant, S. S. Iyengar, J. Tomasi, M. Cossi, J. M. Millam, M. Klene, C. Adamo, R. Cammi, J. W. Ochterski, R. L. Martin, K. Morokuma, O. Farkas, J. B. Foresman, and D. J. Fox, Gaussian 16 Gaussian, Inc., 2016.

[49] A. Kumar, V. Pottiboyina, and M. D. Sevilla,"One-electron oxidation of neutral sugar radicals of 2'-deoxyguanosine and 2'-deoxythymidine: A density functional theory (DFT) study," J. Phys. Chem. B **116**, 9409-9416 (2012).

[50] A. Kumar and M. D. Sevilla,"Proton transfer induced SOMO-to-HOMO level switching in one-electron oxidized A-T and G-C base pairs: A density functional theory study," J. Phys. Chem. B **118**, 5453-5458 (2014).

[51] K. Yamaguchi, F. Jensen, A. Dorigo, and K. N. Houk,"A spin-correction procedure for unrestricted Hartree-Fock and Møller-Plesset wave functions for singlet diradicals and polyradicals," Chem. Phys. Lett. **149**, 537-542 (1988).

[52] T. Saito, S. Nishihara, Y. Kataoka, Y. Nakanishi, T. Matsui, Y. Kitagawa, T. Kawakami, M. Okumura, and K. Yamaguchi,"Transition state optimization based on approximate spin-projection (AP) method," Chem. Phys. Lett. **483**, 168-171 (2009).

[53] T. Saito, S. Nishihara, Y. Kataoka, Y. Nakanishi, Y. Kitagawa, T. Kawakami, S. Yamanaka, M. Okumura, and K. Yamaguchi,"Reinvestigation of the reaction of ethylene and singlet oxygen by the approximate spin projection method. Comparison with multireference coupled-cluster calculations," J. Phys. Chem. A **114**, 7967-7974 (2010).

[54] I. M. Alecu, J. Zheng, Y. Zhao, and D. G. Truhlar,"Computational thermochemistry: Scale factor databases and scale factors for vibrational frequencies obtained from electronic model chemistries," J. Chem. Theory Comput. **6**, 2872-2887 (2010).

[55] E. D. Glendening, J. K. Badenhoop, A. E. Reed, J. E. Carpenter, J. A. Bohmann, C. M. Morales, C. R. Landis, and F. Weinhold, NBO 6.0, Theoretical Chemistry Institute, University of Wiscosin, 2013.

[56] K. A. Linton, T. G. Wright, and N. A. Besley,"Quantum chemical study of the structure, spectroscopy and reactivity of $NO^{+}.(H_2O)_n$ clusters," Phil. Trans. R. Soc. A **376**, 20170152 (2018).

[57] E. Epifanovsky, A. T. B. Gilbert, X. Feng, J. Lee, Y. Mao, N. Mardirossian, P. Pokhilko, A. F. White, M. P. Coons, A. L. Dempwolff, Z. Gan, D. Hait, P. R. Horn, L. D. Jacobson, I. Kaliman, J. Kussmann, A. W. Lange, K. U. Lao, D. S. Levine, J. Liu, S. C. McKenzie, A. F. Morrison, K. D. Nanda, F. Plasser, D. R. Rehn, M. L. Vidal, Z.-Q. You, Y. Zhu, B. Alam, B. J. Albrecht, A. Aldossary, E. Alguire, J. H. Andersen, V. Athavale, D. Barton, K. Begam, A. Behn, N. Bellonzi, Y. A. Bernard, E. J. Berquist, H. G. A. Burton, A. Carreras, K. Carter-Fenk, R. Chakraborty, A. D. Chien, K. D. Closser, V. Cofer-Shabica, S. Dasgupta, M. d. Wergifosse, J. Deng, M. Diedenhofen, H. Do, S. Ehlert, P.-T. Fang, S. Fatehi, Q. Feng, T. Friedhoff, J. Gayvert, Q. Ge, G. Gidofalvi, M. Goldey, J. Gomes, C. E. González-Espinoza, S. Gulania, A. O. Gunina, M. W. D. Hanson-Heine, P. H. P. Harbach, A. Hauser, M. F. Herbst, M. H. Vera, M. Hodecker, Z. C. Holden, S. Houck, X. Huang, K. Hui, B. C. Huynh, M. Ivanov, Á. Jász, H. Ji, H. Jiang, B. Kaduk, S. Kähler, K. Khistyaev, J. Kim, G. Kis, P. Klunzinger, Z. Koczor-Benda, J. H. Koh, D. Kosenkov, L. Koulias, T. Kowalczyk, C. M. Krauter, K. Kue, A. Kunitsa, T. Kus, I. Ladjánszki, A. Landau, K. V. Lawler, D. Lefrancois, S. Lehtola, R. R. Li, Y.-P. Li, J. Liang, M. Liebenthal, H.-H. Lin, Y.-S. Lin, F. Liu, K.-Y. Liu, M. Loipersberger, A. Luenser, A. Manjanath, P. Manohar, E. Mansoor, S. F. Manzer, S.-P. Mao, A. V. Marenich, T. Markovich, S. Mason, S. A. Maurer, P. F. McLaughlin, M. F. S. J. Menger, J.-M. Mewes, S. A. Mewes, P. Morgante, J. W. Mullinax, K. J. Oosterbaan, G. Paran, A. C. Paul, S. K. Paul, F. Pavošević, Z. Pei, S. Prager, E. I. Proynov, Á. Rák, E. Ramos-Cordoba, B. Rana, A. E. Rask, A. Rettig, R. M. Richard, F. Rob, E. Rossomme, T. Scheele, M. Scheurer, M. Schneider, N. Sergueev, S. M. Sharada, W. Skomorowski, D. W. Small, C. J. Stein, Y.-C. Su, E. J. Sundstrom, Z. Tao, J. Thirman, G. J. Tornai, T. Tsuchimochi, N. M. Tubman, S. P. Veccham, O. Vydrov, J. Wenzel, J. Witte, A. Yamada, K. Yao, S. Yeganeh, S. R. Yost, A. Zech, I. Y. Zhang, X. Zhang, Y. Zhang, D. Zuev, A. Aspuru-Guzik, A. T. Bell, N. A. Besley, K. B. Bravaya, B. R. Brooks, D. Casanova, J.-D. Chai, S. Coriani, C. J. Cramer, G. Cserey, A. E. DePrinceIII, R. A. DiStasioJr., A. Dreuw, B. D. Dunietz, T. R. Furlani, W. A. GoddardIII, S. Hammes-Schiffer, T. Head-Gordon, W. J. Hehre, C.-P. Hsu, T.-C. Jagau, Y. Jung, A. Klamt, J. Kong, D. S. Lambrecht, W. Liang, N. J. Mayhall, C. W. McCurdy, J. B. Neaton, C. Ochsenfeld, J. A. Parkhill, R. Peverati, V. A. Rassolov, Y. Shao, L. V. Slipchenko, T. Stauch, R. P. Steele, J. E. Subotnik, A. J. W. Thom, A. Tkatchenko, D. G. Truhlar, T. V. Voorhis, T. A. Wesolowski, K. B. Whaley, H. L. WoodcockIII, P. M. Zimmerman, S. Faraji, P. M. W. Gill, M. Head-Gordon, J. M. Herbert and A. I. Krylov,"Software for the frontiers of quantum chemistry: An overview of developments in the Q-Chem 5 package," J. Chem. Phys. **155**, 084801 (2021).

[58] H. Do and N. A. Besley,"Structural optimization of molecular clusters with density functional theory combined with basin hopping," J. Chem. Phys. **137**, 134106 (2012).

[59] G. K. Jarvis, M. Evans, C. Y. Ng, and K. Mitsuke,"Rotational-resolved pulsed field ionization photoelectron study of NO$^+$(X$^1\Sigma^+$,v$^+$=0–32) in the energy range of 9.24–16.80 eV," J. Chem. Phys. **111**, 3058-3069 (1999).

[60] P. G. Szalay, J. Vazquez, C. Simmons, and J. F. Stanton,"Triplet instability in doublet systems," J. Chem. Phys. **121**, 7624-7631 (2004).

[61] M.-P. Kitsaras and S. Stopkowicz,"Spin contamination in MP2 and CC2, a surprising issue," J. Chem. Phys. **154**, 131101 (2021).

[62] J. W. Linnett,"A modification of the Lewis-Langmuir octet rule," J. Am. Chem. Soc. **83**, 2643-2653 (1961).

[63] D. M. Hirst and M. E. Linington,"Localized orbitals for the oxygen and nitric oxide molecules," Theor. Chem. Acc. **16**, 55-62 (1970).

[64] T. J. Lee and P. R. Taylor,"A diagnostic for determining the quality of single-reference electron correlation methods," Int. J. Quantum Chem., Quantum Chem. Symp. **36**, 199-207 (1989).

[65] D. Jayatilaka and T. J. Lee,"Open-shell, coupled-cluster theory," J. Chem. Phys. **98**, 9734-9747 (1993).

[66] S. Mallick, B. Roy, and P. Kumar,"A comparison of DLPNO-CCSD(T) and CCSD(T) method for the determination of the energetics of hydrogen atom transfer reactions," Comput. Theor. Chem. **1187**, 112934 (2020).

[67] Y. Guo, C. Riplinger, U. Becker, D. G. Liakos, Y. Minenkov, L. Cavallo, and F. Neese,"Communication: An improved linear scaling perturbative triples correction for the domain based local pair-natural orbital based singles and doubles coupled cluster method [DLPNO-CCSD(T)]," J. Chem. Phys. **148**, 011101 (2018).

[68] F. Neese,"Software update: The ORCA program system, version 4.0," WIREs Comput. Mol. Sci. **8**, e1327 (2018).

[69] B. O. Roos, P. R. Taylor, and E. M. Siegbahn,"A complete active space SCF method (CASSCF) using a density matrix formulated super-CI approach," Chem. Phys. **48**, 157-173 (1980).

[70] B. P. Pritchard, D. Altarawy, B. Didier, T. D. Gibson, and T. L. Windus,"New basis set exchange: An open, up-to-date resource for the molecular sciences community," J. Chem. Inf. Model. **59**, 4814-4820 (2019).

[71] K. Andersson, P. A. Malmqvist, and B. O. Roos,"Second-order perturbation theory with a complete active space self-consistent field reference function," J. Chem. Phys. **96**, 1218-1226 (1992).

[72] M. Abe, G. Gopakmar, T. Nakajima, and K. Hirao, in *Radiation induced molecular phenomena in nucleic acids*, edited by K. Shukla, M. K., and J. Leszczynski (Springer, Netherlands, 2008), pp. 157-177.

[73] G. Li Manni, I. Fdez. Galván, A. Alavi, F. Aleotti, F. Aquilante, J. Autschbach, D. Avagliano, A. Baiardi, J. J. Bao, S. Battaglia, L. Birnoschi, A. Blanco-González, S. I. Bokarev, R. Broer, R. Cacciari, P. B. Calio, R. K. Carlson, R. Carvalho Couto, L. Cerdán, L. F. Chibotaru, N. F. Chilton, J. R. Church, I. Conti, S. Coriani, J. Cuéllar-Zuquin, R. E. Daoud, N. Dattani, P. Decleva, C. de Graaf, M. G. Delcey, L. De Vico, W. Dobrautz, S. S. Dong, R. Feng, N. Ferré, M. Filatov, L. Gagliardi, M. Garavelli, L. González, Y. Guan, M. Guo, M. R. Hennefarth, M. R. Hermes, C. E. Hoyer, M. Huix-Rotllant, V. K. Jaiswal, A. Kaiser, D. S. Kaliakin, M. Khamesian, D. S. King, V. Kochetov, M. Krośnicki, A. A. Kumaar, E. D. Larsson, S. Lehtola, M.-B. Lepetit, H. Lischka, P. López Ríos, M. Lundberg, D. Ma, S. Mai, P. Marquetand, I. C. D. Merritt, F. Montorsi, M. Mörchen, A. Nenov, V. H. A. Nguyen, Y. Nishimoto, M. S. Oakley, M. Olivucci, M. Oppel, D. Padula, R. Pandharkar, Q. M. Phung, F. Plasser, G. Raggi, E. Rebolini, M. Reiher, I. Rivalta, D. Roca-Sanjuán, T. Romig, A. A. Safari, A. Sánchez-Mansilla, A. M. Sand, I. Schapiro, T. R. Scott, J. Segarra-Martí, F. Segatta, D.-C. Sergentu, P. Sharma, R. Shepard, Y. Shu, J. K. Staab, T. P. Straatsma, L. K. Sørensen, B. N. C. Tenorio, D. G. Truhlar, L. Ungur, M. Vacher, V. Veryazov, T. A. Voß, O. Weser, D. Wu, X. Yang, D. Yarkony, C. Zhou, J. P. Zobel and R. Lindh,"The OpenMolcas web: A community-driven approach to advancing computational chemistry," J. Chem. Theory Comput. **19**, 6933-6991 (2023).

[74] D. Roca-Sanjuán, M. Rubio, M. Merchán, and L. Serrano-Andrés,"Ab initio determination of the ionization potentials of DNA and RNA nucleobases," J. Chem. Phys. **125**, 084302 (2006).

[75] G. Ghigo, B. O. Roos, and P.-Å. Malmqvist,"A modified definition of the zeroth-order hamiltonian in multiconfigurational perturbation theory (CASPT2)," Chem. Phys. Lett. **396**, 142-149 (2004).

[76] S. Hirata and M. Head-Gordon,"Time-dependent density functional theory within the Tamm–Dancoff approximation," Chem. Phys. Lett. **314**, 291-299 (1999).

[77] J. Liu and L. Cheng,"An atomic mean-field spin-orbit approach within exact two-component theory for a non-perturbative treatment of spin-orbit coupling," J. Chem. Phys. **148**, (2018).

[78] S. Kotaru, P. Pokhilko, and A. I. Krylov,"Spin–orbit couplings within spin-conserving and spin-flipping time-dependent density functional theory: Implementation and benchmark calculations," J. Chem. Phys. **157**, (2022).

[79] B. H. Munk, C. J. Burrows, and H. B. Schlegel,"An exploration of mechanisms for the transformation of 8-oxoguanine to guanidinohydantoin and spiroiminodihydantoin by density functional theory," J. Am. Chem. Soc. **130**, 5245-5256 (2008).

[80] G. Herzberg, *Molecular spectra and molecular structure. I. Diatomic molecules* (Krieger Publishing Company, Malabar, Florida, 1950), 2th edn.,

[81] W. Lu and J. Liu,"Capturing transient endoperoxide in the singlet oxygen oxidation of guanine," Chem. Eur. J. **22**, 3127-3138 (2016).

[82] J. Troe," Statistical adiabatic channel model of ion-neutral dipole capture rate constants," Chem. Phys. Lett. **122**, 425-430 (1985).

[83] C. Larriba-Andaluz and C. J. Hogan, Jr.,"Collision cross section calculations for polyatomic ions considering rotating diatomic/linear gas molecules," J. Chem. Phys. **141**, 194107 (2014).

[84] J. Benny, T. Saito, M. M. Moe, and J. Liu,"Singlet O_2 reactions with radical cations of 8-bromoguanine and 8-bromoguanosine: Guided-ion beam mass spectrometric measurements and theoretical treatments," J. Phys. Chem. A **126**, 68-79 (2022).

[85] M. C. Aragoni, C. Caltagirone, V. Lippolis, E. Podda, A. M. Z. Slawin, J. D. Woollins, A. Pintus, and M. Arca,"Diradical character of neutral heteroleptic bis(1,2-dithiolene) metal complexes: Case study of [Pd(Me_2timdt)(mnt)] (Me_2timdt = 1,3-dimethyl-2,4,5-trithioxoimidazolidine; mnt^{2-} = 1,2-dicyano-1,2-ethylenedithiolate)," Inorg. Chem. **59**, 17385-17401 (2020).

[86] J. W. Verhoeven,"On the role of spin correlation in the formation, decay, and detection of long-lived, intramolecular charge-transfer states," J. Photochem. Photobiol. C **7**, 40-60 (2006).

[87] J. W. Verhoeven, H. J. van Ramesdonk, M. M. Groeneveld, A. C. Benniston, and A. Harriman,"Long-lived charge-transfer states in compact donor–acceptor dyads," ChemPhysChem **6**, 2251-2260 (2005).

[88] Y. Hou, I. Kurganskii, A. Elmali, H. Zhang, Y. Gao, L. Lv, J. Zhao, A. Karatay, L. Luo, and M. Fedin,"Electronic coupling and spin–orbit charge transfer intersystem crossing (SOCT-ISC) in compact bdp–carbazole dyads with different mutual orientations of the electron donor and acceptor," J. Chem. Phys. **152**, 114701 (2020).

[89] H. Cao, I. Kurganskii, J. Pang, R. Duan, J. Zhao, M. Fedin, M.-D. Li, and C. Li,"Charge transfer, intersystem crossing, and electron spin dynamics in a compact perylenemonoimide-phenoxazine electron donor–acceptor dyad," J. Phys. Chem. B **125**, 12859-12875 (2021).

[90] R. A. Marcus,"Unimolecular dissociations and free radical recombination reactions," J. Chem. Phys. **20**, 359-364 (1952).

[91] L. Zhu and W. L. Hase, A general rrkm program (QCPE 644), quantum chemistry program exchange, Chemistry Department, University of Indiana, 1993.

[92] T. Beyer and D. F. Swinehart,"Algorithm 448: Number of multiply-restricted partitions," Commun. ACM **16**, 379 (1973).

[93] M. T. Rodgers, K. M. Ervin, and P. B. Armentrout,"Statistical modeling of collision-induced dissociation thresholds," J. Chem. Phys. **106**, 4499-4508 (1997).

[94] A. N. Bridgers, J. A. Urquilla, J. Im, and A. S. Petit,"Theoretical study of the photochemical mechanisms of the electronic quenching of NO($a^2\Sigma^+$) with CH_4, CH_3OH, and CO_2," J. Phys. Chem. A **127**, 7228-7240 (2023).

[95] X. Lu, C. Shang, L. Li, R. Chen, B. Fu, X. Xu, and D. H. Zhang,"Unexpected steric hindrance failure in the gas phase $F^- + (CH_3)_3CI$ S_N2 reaction," Nat. Commun. **13**, 4427 (2022).